OULUN YLIOPISTO
UNIVERSITY of OULU

DEGREE PROGRAMME IN ELECTRICAL ENGINEERING

MASTER'S THESIS

X-RAY DIFFRACTION STUDIES OF VO_2 THIN FILMS

Author	Tero Timonen
Supervisor	Jyrki Lappalainen
Second Examiner	Matti Kangaspuoskari

September 2014

Timonen T. (2014) X-Ray Diffraction Studies of VO_2 Thin Films. University of Oulu, Department of Electrical Engineering. Master's Thesis, 68 p.

ABSTRACT

The aim of this work is to investigate the effect of strain in vanadium dioxide (VO_2) thin films. Vanadium dioxide undergoes a metal-insulator transition involving radical changes in the electrical conductivity, and strain is one of the parameters which can influence the transition characteristics. In form of a thin film, vanadium dioxide is subjected to strain which arises from the lattice mismatch between the substrate and the film. To study the effect of strain, a set of vanadium dioxide thin films with thickness from 20 to 240 nm were grown using pulsed laser deposition method, and the structure of the films were characterized using X-ray diffraction. The surface morphology of the thin films was also examined using atomic force microscopy.

In the insulating state, the films were composed of both M_1 and M_2 phases of vanadium dioxide. The transition was observed to be controlled by M_2 phase in films which were thinner than 100 nm and by M_1 phase in thicker films. The presence of M_2 phase was caused by strain. The metal-insulator transition occurred at much wider temperature range in thinner films which were more strained than the thicker films showing more abrupt transitions. The relaxation of the strain in thicker films resulted in misorientation of the crystallites and caused the surface roughness to increase with the film thickness.

Key words: vanadium dioxide, metal-insulator transition, thin film, strain, x-ray diffraction

Timonen T. (2014) VO_2 ohutkalvojen röntgendiffraktiotutkimuksia. Oulun yliopisto, Sähkötekniikan osasto. Diplomityö, 68 s.

TIIVISTELMÄ

Tämän työn tarkoituksena on tutkia venymän vaikutusta vanadiinidioksidi (VO_2) ohutkalvoissa. Vanadiinidioksidissa ilmenevä metalli-eriste transitio aiheuttaa suuria muutoksia aineen sähkönjohtavuudessa ja venymän on huomattu vaikuttavan transition ominaisuuksiin. Ohutkalvomuodossa vanadiinidioksidiin kohdistuu venymä, joka aiheutuu kalvon ja substraatin hilavakioiden epäsovituksesta. Venymästä aiheutuvien vaikutusten selvittämiseksi eri paksuisia (20 – 240 nm) vanadiinidioksidi ohutkalvoja valmistettiin pulssilaserkasvatuksella ja niiden rakennetta karakterisoitiin röntgendiffraktiolla. Myös ohutkalvojen pinnanmuotoa tutkittiin atomivoimamikroskopian avulla.

Eristetilassa kalvot koostuivat vanadiinioksidin M_1 ja M_2 faaseista, ja M_2 faasin huomattiin kontrolloivan transitiota kalvoissa, jotka olivat ohuempia kuin 100 nm, kun taas paksuimmissa kalvoissa transitiota kontrolloi M_1 faasi. M_2 faasin mukanaolo johtui venymästä. Metalli-eriste transitio tapahtui laajemmalla lämpötila-alueella ohuimmissa kalvoissa, joissa venyminen oli suurempaa kuin paksummissa kalvoissa. Paksuimmissa kalvoissa transitio olikin paljon voimakkaampi. Venymän relaksoituminen paksuimmissa kalvoissa johti kiteiden kallistumiseen aiheuttaen sen, että pinnan karheus kasvoi kalvon paksuuden mukana.

Avainsanat: vanadiinidioksidi, metalli-eriste transitio, ohutkalvo, venymä, röntgendiffraktio

TABLE OF CONTENTS

FOREWORD

A lot of water has run in the river Iijoki since the beginning of my studies, but now the time has come to conclude this period in my life. Though a long road has been travelled thus far, I feel the journey has just begun. I don't know where the path will lead from here on, but I am ready for the next step.

This work was done in the Microelectronics and Materials Physics laboratories at the University of Oulu. I want to thank my supervisor Prof. Jyrki Lappalainen for giving me the opportunity to work on this thesis. Thanks also to my second examiner Lic.Sc. (Tech.) Matti Kangaspuoskari for participating in the project. It has certainly been instructive in many ways. I give my appreciations also to Joni Huotari for getting me started with the pulsed laser deposition experiments for my thesis, as well as all the other guidance I have received. X-ray diffraction has been of great importance in my thesis, and I'm very grateful to Jarkko Puustinen for the help and advices related to the XRD and the other measurements.

The last and most important words of gratitude I dedicate to my family for all the love and support you have given me during the years. It means more to me than words can ever describe.

Oulu, September 21st, 2014

Tero Timonen

LIST OF ABBREVATIONS AND SYMBOLS

3D	Three-dimensional
AFM	Atomic force microscopy
BC	Bandwidth control
FC	Filling control
FWHM	Full width at half maximum
GIXRD	Grazing incidence X-ray diffraction
LCAO	Linear combination of atomic orbitals
LDA	Local-density approximation
LPA	Line profile analysis
MCM	Monoclinic and correlated metal
MIT	Metal-insulator transition
NFE	Nearly free electron
PLD	Pulsed laser deposition
RMS	Root mean square
RSM	Reciprocal space map
SMT	Semiconductor-to-metal transition
SPM	Scanning probe microscopy
SPT	Structural phase transition
STM	Scanning tunneling microscope
XAS	X-ray absorption spectroscopy
XRD	X-ray diffraction

A_{α}	Absorption factor for GIXRD geometry
$A_{\theta\text{-}2\theta}$	Absorption factor for θ-2θ geometry
a	Lattice constant
a_L	Free lattice parameter of the film
a_S	Free lattice parameter of the substrate
$a_{\perp}$	Out-of-plane lattice parameter of the film
$a_{\parallel}$	In-plane lattice parameter of the film
a_1, a_2, a_3	Base vectors
B_1	Width of the $3d_{\pi}^{*}$ band
b_1, b_2, b_3	Reciprocal base vectors
c	Velocity of light
d_{hkl}	Interplanar spacing
E	Total energy
E_g	Energy gap
F_{hkl}	Unit cell structure factor
$F(Q)$	Scattering amplitude
f	Frequency
$f^0(Q)$	Atomic form factor
G_{hkl}	Reciprocal lattice vector
ΔH	Latent heat of the metal-insulator transition
h	Planck constant
$\hbar$	Reduced Planck constant
$hkil$	Miller indices
I	Current
$I(l_t)$	Intensity at a distance l_t

I_0	Intensity of the incoming radiation
k	Wave vector of the incident wave
k'	Wave vector of the scattered wave
k_α	Correction factor of the absorption factor for GIXRD geometry
l	Orbital quantum number
l_f	Film length
l_t	Path length
m	Mass
m_e	Mass of electron
m_l	Magnetic quantum number
m_s	Spin magnetic quantum number
N_p	Number of primitive cells
N_u	Number of unit cells
n	Principal quantum number
n_f	Band filling parameter
p	Momentum
Q	Scattering vector
Q_x	X component of the scattering vector
Q_z	Z component of the scattering vector
q_e	Elementary charge
R	Resistance
R_q	Root mean square roughness
R_p	Relaxation parameter
R_n	Lattice vector
r	Interatomic separation
r_l	Position of atom in crystal
r_j	Position of atom in unit cell
r_0	Scattering length
T_{cool}	Transition temperature upon cooling
T_{MIT}	Transition temperature upon heating
t	Hopping interaction parameter
t_c	Critical thickness
t_f	Film thickness
U	Voltage
U_c	Correlation energy
V	Potential energy
$V(r)$	Lennard-Jones potential
w	Film width
Z	Atomic number
α	Angle between a_2 and a_3
α_f	Exit angle
α_i	Incident angle
β	Angle between a_1 and a_3
γ	Angle between a_1 and a_2
Δ	Charge-transfer energy
δ_L	Relative lattice mismatch
$\delta_\perp$	Vertical lattice mismatch
$\delta_\parallel$	Lateral lattice mismatch

ε	Strain
ε_0	Vacuum permittivity
θ	Scattering angle
θ_B	Bragg angle
λ	Wavelength
μ	Linear attenuation coefficient
ρ	Resistivity
$\rho(r)$	Charge distribution
σ	Uniaxial stress
$\tau_{1/e}$	Penetration depth
ψ	Wave function
$\psi_k(x)$	Bloch wave function
Ω	Inclination angle of the scattering vector
ω	Inclination angle of the sample

1. INTRODUCTION

Modern electronics require components of reduced size in order to fulfill the ever-growing demand of system miniaturization that enables higher functional density. At the same time, the performance and reliability of the devices must be enhanced. This requires advanced materials with optimized properties for given assignment. Materials science is a scientific field which deals with the synthesis of materials with different structures and properties. Atoms are the basic building blocks that construct the materials, and because atoms can combine with other atoms in numerous ways, the properties they exhibit is extremely diverse. The diversity is further increased due to the sophisticated methods which are developed to produce novel materials and structures with great complexity in thin film and nanosized forms. Owing to the size reduction, these materials can exhibit properties which are not met in their bulk counterparts.

Structural characterization of materials is highly important since the physical properties are strongly interlinked to their microstructure. X-ray diffraction (XRD) can be used to investigate the inner structure of solid state materials because the diffraction phenomenon is directly related to their atomic content. When X-rays are scattered from the atoms, the waves interfere destructively or constructively depending on the atomic distances. The condition for the constructive interference, *i.e.* diffraction, is given by the famous Bragg's law. Strain induces changes in the lattice parameters, and as a result, alters the condition for diffraction. In thin films, the difference between the lattice parameters of the substrate and the film causes strain which may influence the properties of the film. Owing to the advancements in the equipment, X-ray diffraction can nowadays be performed in high-resolution allowing one to detect the small changes in lattice parameters and study the strain in thin films.

Vanadium dioxide (VO_2) is a widely studied material because of its well-known metal-insulator transition (MIT) which occurs near room temperature. MIT in VO_2 is accompanied by a structural phase transition from a low-temperature insulating phase to a high-temperature metallic phase. The exact physical origin of this phenomenon has been the subject of intense debate in the scientific community since its discovery. A lot of effort has also been made to relate MIT characteristics to the microstructure in order to tune the transition properties for specific applications. Strain is one of the features which are observed to significantly modify MIT characteristics, especially the transition temperature. The emphasis in this thesis is to investigate the impact of strain in VO_2 thin films which are 20 – 240 nm thick by means of X-ray diffraction and correlate the results to MIT characteristics.

The first main chapter of this thesis gives a general view of solid-state physics. The next chapter is dedicated to cover the background of metal-insulator transitions with the focus on the transition in vanadium dioxide. In the following chapter, the physical basis of X-ray diffraction and the related measurement procedures utilized in this work are explained. After that, the techniques utilized in the growth and other characterizations of the thin films are shortly presented. Then all the results are summarized in Chapter 7 followed by a discussion where the results are overviewed. Finally, the thesis is concluded, and the cited literature is listed in the references.

2. STRUCTURE OF SOLID STATE MATERIAL

2.1. Quantum Mechanics

Atoms are formed of nucleus, which is constructed of protons and neutrons, and electrons orbiting around the nucleus. The different orbits where electrons reside around the nucleus have discrete energies. This quantization of certain physical properties is one of the phenomena explained in the framework of quantum mechanics. In quantum mechanics, the properties of a particle, such as an electron, are described by using a wave function ψ. The concept of a wave function is abstract, but it allows one to mathematically obtain physical quantities related to the particle. This can, however, only be achieved in the limits of Heisenberg's uncertainty principle.

The wave function treats particles as waves. This wave-particle duality is another important character of quantum mechanics. The wave-particle duality considers moving particles to behave also as waves and that waves, such as electromagnetic radiation, have also particle characteristics. The de Broglie wavelength λ of a particle is associated to its momentum p in the following way

$$\lambda = \frac{h}{p} = \frac{h}{mv}, \tag{1}$$

where h is the Planck constant, m is the relativistic mass, and v is the velocity of the particle. The particle's momentum can be described using a concept of wave vector k as presented in equation (2).

$$p = \frac{h}{\lambda} = \frac{h}{2\pi}\frac{2\pi}{\lambda} = \hbar k\,, \tag{2}$$

where $\hbar$ is the reduced Planck constant. In quantum mechanics, the reduced Plank constant is the unit of angular momentum [1].

While the momentum and other quantities can be derived from the wave function by using a suitable operator, the wave function itself is derived from Schrödinger's equation. The Schrödinger's equation is a fundamental equation of quantum mechanics. The steady-state, *i.e.* time-independent, form of Schrödinger's equation in one dimension is

$$\frac{\partial \psi}{\partial x^2} + \frac{2m}{\hbar^2}(E - V)\psi = 0\,, \tag{3}$$

where E is the total energy of the particle and V is its potential energy. There can be multiple solutions, *i.e.* wave functions, and they each correspond to a specific value of energy. These wave functions, denoted as ψ_n, are called eigenfunctions and the corresponding energies E_n are called eigenvalues. The term n is thereby related to the quantization of energy, and it's called the principal quantum number. For an electron which is bound to an atom by electric field, the discrete values of energies are negative, but in the case of an ionized atom, the energies of an electron may have any positive value. [1]

To fully describe an electron in an atom, three other quantum numbers besides n are needed, and they arise from the restricted motion of negatively charged electron around positively charged nucleus. These are the orbital quantum number l, the magnetic quantum number m_l, and the spin magnetic quantum number m_s. The orbital quantum number is related to the quantization of angular-momentum magnitude whereas the quantization of its direction is specified by the magnetic quantum number. [1]

Possible values of the quantum numbers are given in Table 1.

Table 1. Quantum numbers of an atomic electron

Name	Symbol	Possible Values	Notation
Principal	n	1, 2, 3, 4, …	K, L, M, N, …
Orbital	l	0, 1, 2, …, (n-1)	s, p, d, f, …
Magnetic	m_l	0, ±1, ±2, …, ±l	-
Spin magnetic	m_s	±1/2	-

Even though the angular momentum, specified by l and m_l, can be zero, the electron will always have an intrinsic angular momentum called spin. Its magnitude is always the same, but it may have two orientations. [1]

The electrons in an atom occupy different shells which constitute of subshells and orbitals. These are defined by the principal, orbital, and magnetic quantum number, respectively. The shells and the subshells are usually labeled using the notation given in Table 1. The occupation of these states is, however, restricted because of the Pauli exclusion principle. The Pauli principle states that there can be only one electron having the same four quantum numbers, and therefore the maximum possible number of electrons in a shell n can be $2n^2$. For a neutral atom, the total number of atomic electrons equals to the atomic number Z, *i.e.* to the number of protons in nucleus. The distribution of electrons in different orbits is expressed by means of electron configuration. Lithium, for example, has an electron configuration of $1s^2\,2s^1$ in which the first number identifies the shell and the letter with a subscript denotes the number of electrons in a subshell l. Because the first shell is full, it is said to be closed. The second shell is the outermost occupied shell which is called the valence shell.

The quantum numbers can also be seen to represent discrete energies in the form of energy levels or states. In a ground state, electrons are always situated in the lowest energy levels permitted by the Pauli principle because of the principle of minimum energy. The levels are, however, not always regularly filled with increasing quantum numbers as seen in transition metals which have a peculiar filling of the shells. Electrons can also make transitions between different energy levels. The case where an electron shifts to a higher energy state is called an excitation since the energy of an atom is increased compared to the ground state. This excited state is usually very unstable, and the electron will shortly return to the ground state or a lower energy state if it's available. The energy difference between these states is then transformed to some form of energy because of the law of conservation of energy. However, not all transitions are possible, *i.e.* there exists forbidden and allowed transitions. These are determined by quantum mechanical selection rules which are based upon conservation laws. Since there are different phenomena how the transition can occur, specific rules are obeyed.

2.2. Crystallography

Only rare elements exist in nature as individual atoms but are rather combined with other atoms. This occurs because the energy of a system consisting of multiple atoms together can be smaller than it would be if the atoms are separated [2]. Between the atoms, electrostatic forces appear because their electrons interact with each other and with the neighbor's nucleus [2]. Attractive interaction is entirely responsible for cohesion in solids, and it takes place between the negatively charged electrons and the positively charged nucleus whereas repulsive interaction occurs because of the Pauli principle and the repulsion between the atoms' charge distributions [3]. The strength of this Coulomb interaction depends on the interatomic separation r, and its influence on the potential energy of the system is expressed by Lennard-Jones potential

$$V(r) = -\frac{A}{r^a} + \frac{B}{r^b}, \tag{4}$$

where the negative term with constants A and a represents the attraction, and the second term with constants B and b represents the repulsion between the atoms [2]. The minimum value and the corresponding location in equation (4) define the bonding energy and the interatomic separation in equilibrium, respectively [2].

The atoms can be distributed in different ways in a solid. In crystalline solids, the atoms are arranged in a highly ordered manner. Because of the periodicity of the atomic arrangement, crystalline solids exhibit so-called long-range order in their structure. In the structure of polycrystalline and amorphous solids, the long-range order isn't preserved, but they still exhibit short-range order. Polycrystalline solids are composed of microscopic crystals, called grains, which vary in size and orientation, and are separated by grain boundaries.

The periodic arrangement of atoms, which defines the crystal structure, can be expressed by means of lattice and basis. Basis is a group of atoms belonging to the material itself and which can be repeated throughout the entire structure according to the lattice. Lattice is an array of points in space to which the basis can be associated, thus constructing the crystal structure of the material. The lattice points can be presented as

$$R_n = n_1 a_1 + n_2 a_2 + n_3 a_3, \tag{5}$$

where R_n is the lattice vector, n_1, n_2, and n_3 are integers, and a_1, a_2, and a_3 are base vectors. A primitive cell is the smallest volume of a parallelepiped defined by the base vectors, and it contains only one lattice point. Usually a unit cell, which can contain more than one lattice point, is used to describe the lattice. Unit cell is the smallest and most symmetric cell which can be used to reproduce the whole crystal. The vectors forming the unit cell are called unit cell axes or crystal axes. The lengths of the vectors are called lattice constants. The unit cell is characterized by its lattice parameters comprising of the length of the vectors and angles between them. Overall, 7 lattice systems based on the shape of the unit cell and 4 types of unit cells exist. Taking into account all the three-dimensional (3D) lattices which are symmetrically different, 14 so-called Bravais lattices exist. Considering all the possible crystal symmetries, there are 230 possible crystal structures, *i.e.* space groups. The 7 lattice systems and the corresponding lattice parameters are summarized in Table 2.

Table 2. Three-dimensional lattice systems

Lattice System	Lattice Parameters		Bravais Lattices
	Crystal Axes	Angles[1]	
Cubic	$a_1 = a_2 = a_3$	$\alpha = \beta = \gamma = 90°$	P (Primitive)
			I (Body-centered)
			F (Face-centered)
Hexagonal	$a_1 = a_2 \neq a_3$	$\alpha = \beta = 90°, \gamma = 120°$	P (Primitive)
Monoclinic	$a_1 \neq a_2 \neq a_3$	$\alpha = \gamma = 90° \neq \beta$	P (Primitive)
			C (Base-centered)
Orthorhombic	$a_1 \neq a_2 \neq a_3$	$\alpha = \beta = \gamma = 90°$	P (Primitive)
			I (Body-centered)
			C (Base-centered)
			F (Face-centered)
Rhombohedral	$a_1 = a_2 = a_3$	$\alpha = \beta = \gamma \neq 90°$	P (Primitive)
Tetragonal	$a_1 = a_2 \neq a_3$	$\alpha = \beta = \gamma = 90°$	P (Primitive)
			I (Body-centered)
Triclinic	$a_1 \neq a_2 \neq a_3$	$\alpha \neq \beta \neq \gamma \neq 90°$	P (Primitive)

[1)] α is angle between a_2 and a_3, β is the angle between a_1 and a_3, and γ is the angle between and a_1 and a_2.

It's a common convention to label a particular crystal plane using Miller indices (*hkl*). The three indexes, *h*, *k*, and *l*, are found in the following way. First the intercepts of the plane in the crystal axes are inverted. Then these reciprocal values are converted into smallest set of integers. If the plane doesn't intercept some of the axes, the corresponding index would be zero since it is the reciprocal value of infinity. Once the Miller indices for planes have been obtained, they can be used to calculate angles between planes as well as spacing between parallel planes. For the simplest and most symmetric structure, *i.e.* the cubic structure, the spacing between adjacent planes (*hkl*) is given by

$$d_{hkl} = \frac{a}{\sqrt{h^2 + k^2 + l^2}}, \tag{6}$$

where *a* is the lattice constant.

Directions in crystals can be designated considering the projection of the direction on the crystal axes and converting them to smallest integers. These integers are labeled as [*hkl*]. The direction [*hkl*] is always perpendicular to the plane (*hkl*) in the case of a cubic structure. Negative indexes are written with bar on top of the corresponding index. For hexagonal structure, crystal planes and directions are usually expressed with four indexes, *h*, *k*, *i*, and *l*. The third index *i* comes from the complement of the sum of *h* and *k*. Therefore, the sum of the first three indexes is always zero.

The lattice can also be presented in reciprocal space. This reciprocal lattice is a Fourier transform of the direct lattice. Such as the lattice in real space was described using base vectors a_1, a_2, and a_3, which specify the direct lattice, the reciprocal lattice is specified by reciprocal base vectors b_1, b_2, and b_3. The base vectors are converted into reciprocal space in the following way

$$b_1 = 2\pi \frac{a_2 \times a_3}{a_1 \cdot a_2 \times a_3},\ b_2 = 2\pi \frac{a_1 \times a_3}{a_1 \cdot a_2 \times a_3},\ b_3 = 2\pi \frac{a_1 \times a_2}{a_1 \cdot a_2 \times a_3}, \tag{7}$$

where the denominator is the volume of the parallelepiped defined by base vectors. The scaling of the reciprocal lattice base vectors with 2π serves a purpose in the examination of the diffraction phenomenon. The reciprocal lattice points can now be presented as

$$G_{hkl} = hb_1 + kb_2 + lb_3, \tag{8}$$

where G_{hkl} is the reciprocal lattice vector which is normal to the plane (*hkl*). In addition, its magnitude is inversely proportional to the spacing between the planes in the following manner

$$|G_{hkl}| = \frac{2\pi}{d_{hkl}}. \tag{9}$$

2.3. Formation of Energy Bands

Atoms in solids are so close to each other that the discrete energy levels of electrons described by wave functions ψ_n overlap. This means that the levels, which previously belonged to the individual atoms, become common to the atoms constituting the solid. When considering the consequences of the overlapping, the Pauli principle becomes important. Since the number of electrons in an orbital is restricted because of the principle, the discrete levels are ought to split to new levels with different energies. The amount of energy splitting depends on the closest interatomic distance in the solid [2].

While the free electron model can explain many properties of metals, it cannot make distinctions between metals, semimetals, semiconductors, and insulators. In the nearly free electron model (NFE model), the free electron model has been extended to take into account the periodic lattice of the solid. In the model, the periodic potential of the ion cores is considered to perturb the band electrons only weakly. The most important property that arises is the possibility of a band gap, also known as the energy gap. This is a forbidden region in energy which separates the energy bands in which the electrons in a crystal are arranged. In a band gap, no wavelike electron orbitals are allowed, and it occurs because the conduction electron waves interact with the ion cores of the crystal. [3]

The potential energy of an electron inside a crystal is periodic with periodicity of the lattice constant *a* of the crystal and can be expressed as

$$V(x) = V(x + ma), \tag{10}$$

where *m* is an integer. Inserting this into Schrödinger equation, it can be shown that the wave functions that solve the equation are of the form

$$\psi_k(x) = V_k(x) e^{ik \cdot x}, \tag{11}$$

where $V_k(x)$ is a periodic function that depends on the potential energy whereas the exponential function represents a travelling wave. The solutions are called Bloch wave functions, and they represent the electron wave functions in a crystal.

Altogether, the Block function is a travelling wave that is modulated by $V_k(x)$ which has the same periodicity a of crystal lattice as $V(x)$. The different solutions of a particular ψ_k are characterized by values of k_n, and they represent a state with an energy E_k which is allowed to exist in the crystal. When these states are very close to each other, they can be considered to form a continuous range of energies, *i.e.* energy bands. Between these allowed states, a forbidden region for which no solutions $\psi_k(x)$ exist might be present. [2]

Because of the forbidden region, an E-k diagram shows discontinuities which occur at values

$$k = \pm\frac{1}{2}G = \pm m\frac{\pi}{a}, \tag{12}$$

where G is a reciprocal lattice vector and m is an integer. This is known as Bragg reflection, and it's the cause of energy gaps. At Bragg reflection, the electron waves in a crystal are diffracted so the wave functions are not travelling waves but standing waves. The allowed regions restricted by the k values are called Brillouin zones, and the first Brillouin zone is the area between $\pm\pi/a$. [3]

In each energy band, there are $2N_p$ orbitals. N_p is the number of primitive cells in a crystal, each of which contributing one independent value of k to each band. Because there can be two orientations of electron spin, the total number of orbitals in a band is twice the number of primitive cells that construct the crystal. [3]

A general view of the band structures in materials showing different electrical behavior is presented in Figure 1.

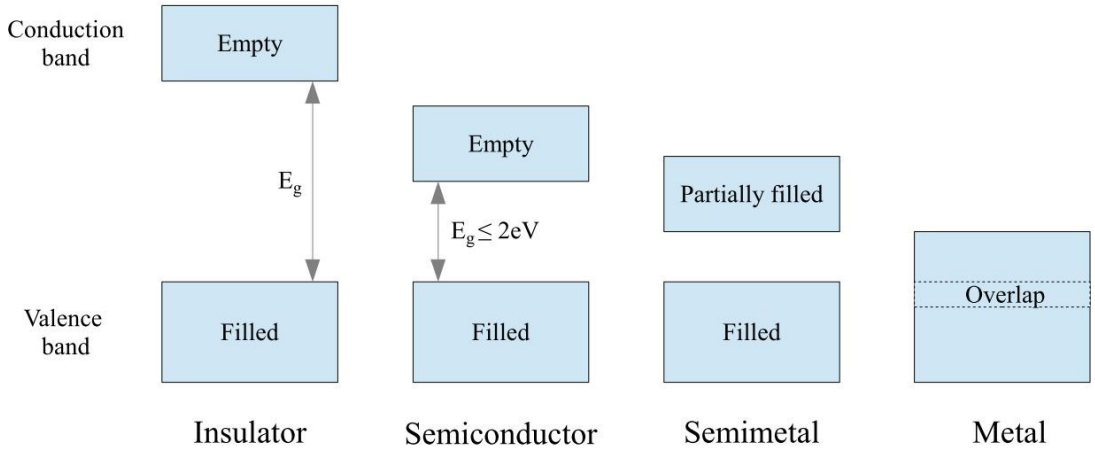

Figure 1. Electronic band structures at 0 K.

The distinction between an insulator and a semiconductor lies in the width of the energy gap E_g. For a semiconductor, the energy difference between the valence band and the conduction band is small enough for electrons to be thermally excited and therefore to conduct current. Semimetals also have a small band gap as in semiconductors, but the conduction band is partially filled even at 0 K. The overlapping of the bands is responsible for the high conductivity in metals.

In solids, the distance between the atoms is large compared to innermost energy levels which therefore stay mainly intact. The electrons occupying these core levels are strongly localized in space and retain this localization even when the free atoms are brought together to form a crystal [4]. To describe their largely retained

properties, a procedure known as the linear combination of atomic orbitals (LCAO) is used [4]. This is also known as the tight-binding approximation [3]. It is considered to be suitable for the inner electrons of atoms, and it is used to describe the *d*-bands of the transition metals [3]. The localized electrons can also contribute to conduction of current by hopping from one localized state to another [4]. The electrical transport occurring this way is known as the hopping conduction, and it results from tunneling effect which requires that the wave functions of the states overlap [4]. There is also another hopping mechanism, called Poole-Frenkel hopping, which doesn't require tunneling.

2.4. Strain in Thin Films

Epitaxial thin films exhibit a high degree of crystalline perfection since the crystal lattice of the underlying single crystal substrate is intended to extend into the layer as so-called pseudomorphic growth. Some deviations from the perfect crystal structure are, however, to be expected in these epilayers. In the majority of epitaxy processes, the growth is heteroepitaxial since the compound is distinct from the substrate meaning that the lattice constants and even the crystallographic structures differ. [5]

When films are epitaxially grown on a crystalline substrate, the film-substrate system is always influenced by strain. The lattice matching at the interference of the substrate and the film causes lattice deformation due to the differences in the free lattice parameters of the film and the substrate. This deformation occurs perpendicular to the interference to minimize the strain energy of the film. If the substrate can be assumed to be infinitely thick compared to the film, the strain energy of the substrate can be neglected and the lattice strain impacts the layer only. By the influence of strain, for example, an initially cubic material can become tetragonally deformed. This occurs, for example, in thin semiconductor layers which are epitaxially grown onto (001) cubic substrates for micro- and optoelectronic applications. [6]

The measure for the strain ε is called mismatch δ_L, and it is the difference between the lattice parameters of the film and the substrate [5]. The relative lattice mismatch between both cubic lattice parameters is

$$\varepsilon = \delta_L = \frac{\Delta a}{a_S} = \frac{a_L - a_S}{a_S}, \tag{13}$$

where a_L and a_S are the free lattice parameters of the film and the substrate, respectively [5, 6]. It has been observed that if the relative mismatch is less than about 14 %, the growth proceeds epitaxially [5]. However, heteroepitaxy will inevitably induce strain despite the precise mismatch value [5].

The lattice distortion can be expressed in terms of the vertical and lateral lattice mismatches, called misfits, according to equations (14) and (15), respectively [6].

$$\delta_\perp = \frac{a_\perp - a_S}{a_S}, \tag{14}$$

$$\delta_\parallel = \frac{a_\parallel - a_S}{a_S}, \tag{15}$$

where $a_\perp$ and $a_\parallel$ are, respectively, the out-of-plane and in-plane lattice parameters of the film [6]. When $a_\parallel = a_S$ holds, the layer is in a fully strained state [5]. In this case, the film growth is pseudomorphic on the substrate as long as the film thickness doesn't exceed certain value [6]. This value is named as critical thickness t_c above which misfit dislocations are formed [6]. Misfit dislocations are formed to accommodate the interfacial strain via mechanical relaxation [5]. This relaxation occurs above a certain threshold of strain, and the film becomes partially or fully relaxed so that $a_\parallel \neq a_S$ now holds [5].

The degree of relaxation can be defined by means of relaxation parameter R_p as presented in equation (16) [5, 6].

$$R_p = \frac{a_\parallel - a_S}{a_L - a_S} \tag{16}$$

R_p takes values between 0 and 1 according to whether the film is in a fully strained state or in a fully relaxed state, respectively [5]. When $R = 0$, the in-plane lattice constant equals to that of the substrate whereas $R = 1$ holds when the in-plane lattice parameter equals to that of the unstrained layer [5]. The degree of strain and associated dislocation densities are important since they can have an impact on the electrical properties of the layer [5].

Figure 2 depicts two cases where the misfit between the substrate and the film causes tetragonal distortion in the unit cell of the film. The lattice constant of the film is larger in a) and smaller in b) than the lattice constant of the underlying substrate. The left-hand and the right-hand graphics in both a) and b) show the film in a fully strained and fully relaxed state, respectively. The figure has been modified from Pietsch *et al.* [6].

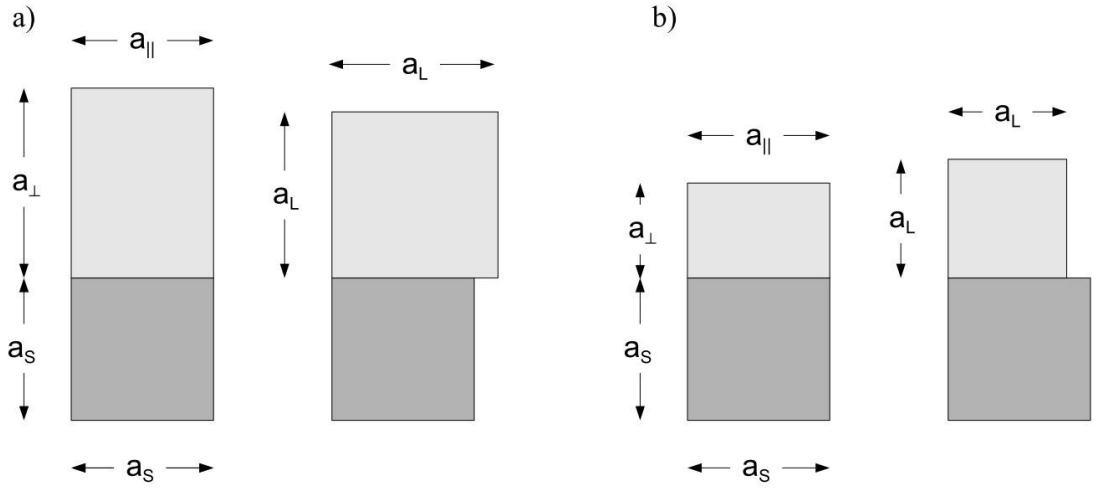

Figure 2. Deformations of lattice structure due to strain.

The positive mismatch in a) induces compressive strain in the lateral direction so that the unit cell expands in the vertical direction. The negative mismatch and the resulting tensile strain in b) will cause the unit cell to shrink in vertical direction.

3. METAL-INSULATOR TRANSITION

3.1. Theory of Metal-Insulator Transition

Metal-insulator transition (MIT) or, alternatively, semiconductor-to-metal transition (SMT) is a widely studied phenomenon which involves an abrupt resistivity change when the material is subjected to change of some variable such as temperature. In addition to thermal triggering, the transition can also be triggered electrically, optically, magnetically, or by strain [7]. MIT is observed in some transition metal oxides which are particularly interesting materials as other MIT-relevant properties, such as colossal magnetoresistance and high-temperature superconductivity, have also been found in these materials [7 - 9]. These materials are referred to as correlated oxides when this kind of anomalous behavior arises due to electron-electron correlation [7, 8]. The conventional band theory, which considers the band structure to be formed solely due to the periodic crystal structure, doesn't take into consideration the possible interaction between electrons [9]. The electrical behavior of some materials therefore differs from that of predicted by the band theory. This was observed, for example, in many transition metal oxides which seemed to be poor conductors even though they should have had partially filled *d*-band (as cited in [9]). The reason for this insulating behavior was then explained to be in electron-electron correlation, which results from the strong Coulomb repulsion between the electrons (as cited in [9]). Mott described a system where a single band, which would normally be formed from the overlap of atomic orbitals, could be split in two as a consequence of strong Coulomb interaction so that the lower band would be full and the system would behave as an insulator (as cited in [9]). When MIT origins from these electron-electron interactions, the transition is referred to as Mott or Mott-Hubbard MIT, and the compound is named Mott-Hubbard insulator to distinguish it from the conventional band insulator [7].

Electron-electron interaction is not the only phenomenon behind MIT. MIT can also originate from electron-lattice interactions, in which case the transition is called Peierls transition and the compound is referred to as Peierls insulator [10]. Peierls transition arises from structural changes in the material which induces lattice deformation [7]. This consequently changes the band structure of the material since the periodic crystal structure is altered by the deformation [7]. Another phenomenon behind MIT is the Anderson localization, which is triggered by disorder [11, 12]. Anderson transition is observed in materials with strong impurity scattering and in materials which are strongly disordered [7]. The disorder causes states in the bands which are localized and delocalized [7]. The states are separated by a mobility edge and are insulating when Fermi level lies in between the band edge and its mobility edge [7].

In order to explain MIT phenomenon, different methods and models have been presented to describe the theory behind it so that it would agree with the experimental results. To treat the correlation effects in *d*-electron systems, a more profound method than the tight-binding approximation is considered to be needed. When the correlation effects are not important, the band structure of metals in a ground state can be calculated using a local-density approximation (LDA) method. Refinements of LDA are, however, necessary to reproduce Mott insulating state and

the anomalous metallic states near the insulating state. The correlation effects have also been considered in a so-called Fermi-liquid theory. [9]

The suitable methods provide a way to calculate the values of some key parameters which are included in some microscopic models [9]. These models and the parameters within are used to describe the material systematics [9]. Two such parameters are used to classify the insulators which do not fit into the description of conventional band theory into two classes [9]. These parameters are U_c, the measure of Coulomb repulsion included in so-called Hubbard model, and Δ, the charge-transfer energy included in so-called *d-p* model [9, 13]. U_c is also known as Hubbard intra-atomic correlation energy [14]. U_c and Δ are the basic parameters that describe the band gaps and the electronic structures in transition metal compounds, and together they make a distinction between Mott-Hubbard-type and a charge-transfer-type insulator [9, 13]. When $U_c > \Delta$, which holds for heavier transition metal compounds, a band gap of a charge-transfer-type is formed whereas Mott-Hubbard insulator is in question when $U_c < \Delta$, and the gap is of *d-d* character [9, 13]. For light transition metal compounds, such as vanadium or titanium compounds, the band gap is a *d-d* gap [13]. The band structures shown in Figure 3 illustrate the difference between Mott-Hubbard and charge-transfer insulators. The figure has been modified from Imada *et al*. [9].

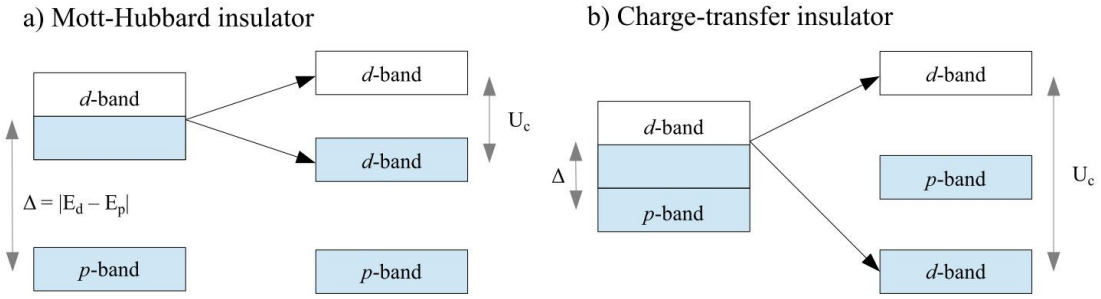

Figure 3. Band structures for a) Mott-Hubbard insulator and b) charge-transfer insulator.

Figure 3a) illustrates the changes in the band structure for Mott-Hubbard insulator as presented in Hubbard model [9]. The *d*-band belongs to the transition metal atoms whereas the *p*-band is that of oxygen atoms of the transition metal oxide compound [9]. The *d*-band is split into a so-called lower and upper Hubbard band as a consequence of *d-d* Coulomb interaction U_c [9]. This generates a charge excitation gap, whose magnitude is proportional to U_c, between them [9, 13]. The gap is then called Mott-Hubbard gap [9]. In contrast, a gap of a *d-p*-type, which is proportional to Δ, is formed in the case of a charge-transfer insulator, as shown in Figure 3b) [9, 13]. The gap is zero for all values of Δ if U_c is zero [13]. Zaanen *et al.* have concluded that a large *d-d* Coulomb interaction is needed but is not sufficient alone to produce a wide band gap in the insulating phase [13].

Hubbard model, in which the transition between Mott-Hubbard insulator and metal is theorized, includes two important parameters that characterize the strongly correlated electron system [9]. These are the electron correlation strength U_c/t and the band filling parameter n_f [9]. t is known as the hopping interaction parameter of the conduction particle [9]. When $n_f = 0$ or $n_f = 2$, the filling is that of a band insulator for a nondegenerate band [9]. When $n_f = 1$, the band is half-filled but the

system can be Mott-Hubbard insulator by the impact of electron correlation [9]. This occurs at some critical value of the electron correlation strength except when the critical value is zero [9]. Transition across this finite value is called the bandwidth control MIT (BC-MIT) [9]. Bandwidth control MIT can be induced by applying external pressure or modifying the internal, *i.e.* chemical, pressure [7, 9]. The internal pressure can be modified by doping the material with substitutional atoms of different sizes [7]. When the filling parameter is not an integer, the system is usually a metal but near $n_f = 1$, an insulating phase may appear, and the transition across this boundary is called the filling control MIT (FC-MIT) [9]. Filling control MIT can be induced by carrier doping [7, 9]. Doping the material with acceptors and donors to modify the doping level, the filling of the band is consequently modified [7]. In addition to bandwidth and filling control, temperature is one of the key parameters that can be controlled to induce MIT [7]. In temperature controlled approach, MIT is simply induced by heating and cooling [7]. Depending on the material system, more than one controllable parameter may be available to induce the transition [7].

3.2. Structure and Metal-Insulator Transition in VO_2

3.2.1. Structure of VO_2

The atomic number of vanadium (V) is 23, and it is a transition metal. The electron configuration of vanadium is $[He]3d^3 4s^2$ so it has partially filled 3*d* and 4*s* subshells. In addition to vanadium dioxide (VO_2), vanadium has many other stable oxides, such as vanadium monoxide (VO), vanadium trioxide (V_2O_3), and vanadium pentoxide (V_2O_5), as well as phases with other oxygen to vanadium ratios. V_2O_3 is an example of Magnéli phases with generic formula V_nO_{2n-1} [15]. MIT is observed in many of the vanadium oxides including, but not limited to, V_2O_3, V_3O_5 and VO_2 [15]. VO_2 has been the subject of intense research as it exhibits MIT near room temperature around 65 - 68 °C in bulk form. In addition to drastic changes in the resistivity, optical properties are substantially modified during the transition, and a great variety of potential applications have been proposed which utilize MIT in VO_2 [7, 8].

The metal-insulator transition in VO_2 is accompanied by a structural phase transition (SPT) from a low-temperature insulating phase to a high-temperature metallic phase. The phase that exhibits metallic behavior above the transition temperature T_{MIT} has a tetragonal unit cell. Since the structure of the metallic phase resembles that of a rutile TiO_2 structure, the phase is known as R phase. In R phase, the vanadium atoms form a body-centered tetragonal lattice and are surrounded by an oxygen octahedron [16]. The insulating phase, which exists below T_{MIT}, has a monoclinic unit cell, and it is known as M_1 phase. Its unit cell is two times larger than that of the metallic phase, and it is formed by the distortion of the tetragonal structure [14, 16]. In M_1, all the vanadium atoms both pair and tilt with respect to the *c*-axis of the tetragonal R phase, *i.e.* c_R-axis [14, 17].

Vanadium dioxide has another monoclinic phase known as M_2 phase. In M_2, half of the vanadium atoms along the c_R-axis pair but do not tilt as in M_1 phase [9, 14, 17]. The other half of the vanadium atoms remain unpaired but tilt perpendicular to c_R forming a zigzag pattern [9, 14, 17]. M_2 can be stabilized, for example, by the application of small uniaxial tension or light doping of VO_2 [17, 18]. M_2 phase is considered to be a local minimum for VO_2 since it can be stabilized by such

minimum perturbations [19]. Uniaxial pressure and doping can also give rise to a triclinic (T) phase, which is considered to be a transitional phase with characteristics of both M_1 and M_2 phases [16, 18, 20]. All the three insulating phases, M_1, M_2, and T, undergo a metal-insulator transition [14].

M_1, M_2, and R phases of VO_2, and their estimated lattice parameters are summarized in Table 3 [17, 21, 22]. The following unit vector relations exist between M_1 and R phase: $a_{M1} \approx 2c_R$, $b_{M1} \approx a_R$, and $c_{M1} \approx a_R - c_R$ [7]. For M_2, $a_{M2} \approx 2a_R$, $b_{M2} \approx 2c_R$, and $c_M \approx a_R$ [17].

Table 3. Lattice parameters for M_1, M_2, and R phases of VO_2

Phase	Space Group	Lattice Parameters	
		Lattice Constants (Å)	Angles
Monoclinic (M_1)	$P2_1/c$	$a = 5.75$, $b = 4.53$, $c = 5.38$	$\alpha = \gamma = 90°$, $\beta = 122.6°$
Monoclinic (M_2)	C2/m	$a = 9.07$, $b = 5.80$, $c = 4.53$	$\alpha = \gamma = 90°$, $\beta = 91.9°$
Tetragonal (R)	$P4_2/mnm$	$a = b = 4.55$, $c = 2.85$	$\alpha = \beta = \gamma = 90°$

3.2.2. Nature of the Transition in VO_2

The nature of the metal-insulator transition in VO_2 has been debated since the discovery of the phenomenon. The existence of other insulating phases than M_1 further complicates the apprehension of MIT in VO_2 [16]. If the structural phase transition induces MIT, the transition in VO_2 has a band-like character and should be classified as Peierls insulator, but if the structural transition is only an accompanying phenomenon of the carrier-induced MIT, VO_2 is labeled as Mott-Hubbard insulator [7, 9]. Based on LDA calculations, Wentzcovitch *et al.* showed that the band theory can find the monoclinic distorted ground state, *i.e.* M_1 phase, with a charge excitation gap and concluded that VO_2 may be more band-like than correlated [23]. These conclusions were opposed by Rice *et al.* since they did not cover the other insulating phases of VO_2 which are considered to be typical Mott-Hubbard insulators [19]. Since M_1 phase can be seen as a superposition of two M_2-typed lattice distortions, the authors stressed that all the three insulating phases, including M_1, are of the same type, *i.e.* Mott-Hubbard insulators [19]. It has been shown, however, that M_2 phase can be described within LDA as well [16]. Experimental results provided by Cavelleri *et al.* also suggest that VO_2 has a band-like character since the atomic arrangement of the high temperature unit cell seems to be essential in the formation of the metallic phase [24].

Experimental results have also given evidence in favor of Mott transition. Kim *et al.* reported that the metal-insulator transition is not driven by the structural phase transition since they do not occur simultaneously. Instead, an intermediate monoclinic and correlated metal (MCM) phase exists between MIT and SPT. The structural phase transition between MCM and the metal phase was induced by Joule heating and the metal-insulator transition was driven by hole carriers in these pump-probe measurements. Originally, the explanation behind Mott transition was theorized in terms of a critical electron carrier density, below which the transition occurs, and the hole-driven MIT brings a new aspect to the phenomenon. [25]

The primary mechanism behind MIT in VO_2 remains disputed since it has features that don't even seem to fit into the description of the conventional Peierls or Mott-Hubbard models. While some calculations provide support that MIT is driven by the critical carrier density and that the electron interactions play a dominant role, others suggest that VO_2 is not a conventional Mott insulator since the Coulomb interactions and the structural distortions interplay in the transition [26, 27]. Spectroscopic studies also support the conclusion that MIT in VO_2 goes beyond the description of both Mott and Peierls transitions, and it may rather be labeled as Mott-Peierls transition [28, 29].

3.2.3. Band Structure of VO_2

In Mott-Hubbard picture, the unusual insulating behavior and the corresponding formation of a band gap stems from the split 3*d* band as a consequence of strong electron-electron interaction as discussed earlier (see Figure 3) [9]. The 3*d* band structure for both the metallic and the insulating phases of VO_2 has been presented by Goodenough, and it is explained as follows (as cited in [16, 30]).

In the metallic phase, the 3*d* states of the V^{4+} ion are first split into e_g and t_{2g} states, and the latter is further split into $3d_{||}$ and the $3d_{\pi}^{*}$ states by the tetragonal crystal field [16, 30]. The $3d_{\pi}^{*}$ and $3d_{||}$ orbitals overlap and are situated around Fermi level, but the $3d_{\pi}^{*}$ band lies higher in energy because it is more hybridized with the O 2*p* orbitals [16, 30]. Because Fermi level now lies within the conduction band, the material exhibits metallic properties.

In the insulating phase, the monoclinic distortion causes changes in the V-O hybridization which upshifts $3d_{\pi}^{*}$ band to even higher energy so that the band now lies above Fermi level and becomes empty [16, 30]. Furthermore, the $3d_{||}$ band, which is aligned along the c_R-axis, is split into a filled and an empty state due to pairing of the V atoms [16, 30]. As a result of these changes, an energy gap is formed between the $3d_{||}$ valence band and $3d_{\pi}^{*}$ conduction band [16, 30]. The majority carriers in the insulating phase are recognized to be of n-type which are thermally activated into the conduction band [31].

The band structures for the insulating and metallic phases are schematically presented in Figure 4, which has been modified from Aetukuri *et al.* and Shin *et al*. The O 2*p* levels are situated well below the V 3*d* states and are not included in the figure. [30, 32]

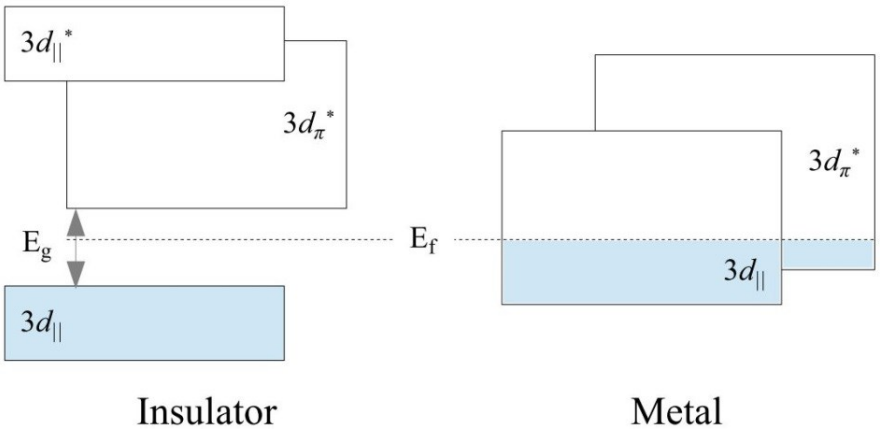

Figure 4. Band structure of VO_2 for the insulating and metallic phases.

The 3*d*-band structure of VO_2 has been well-investigated by Shin *et al.* using spectroscopic methods [30]. They observed clear changes in the 3*d* band across the metal-insulator transition and obtained some energy gap values [30]. In accordance with the description given by Goodenough, Shin *et al.* found the $3d_{\pi}^{*}$ and $3d_{\|}$ states near Fermi level in the metallic phase and observed the rise of the $3d_{\pi}^{*}$ band by about 0.5 eV in the insulating phase [30]. They thought that this band shift may be the driving force of MIT and estimated the band gap to be 0.7 eV [30]. Furthermore, they observed the splitting of the $3d_{\|}$ band and estimated the energy splitting to be about 2.5 eV [30]. The splitting was explained to occur due to strong correlation between the $d_{\|}$-electrons, and the correlation energy U_c was estimated to be about 2.1 eV [30]. Using ultrafast electron microscopy, Grinolds *et al.* have also observed the opening of a band gap caused by splitting of the $3d_{\|}$ band in the insulating phase, which occurs in ultrashort time scale [21].

Originally, Goodenough proposed that MIT in VO_2 stems from the increased *p-d* overlap due to distortion of the VO_6 octahedra and that the change in the symmetry of the structure would split the $3d_{\|}$ band (as cited in [16]). Hence, the reason for the opening of the band gap would be in the electron-lattice interaction [16]. In contrast, Zylbersztejn and Mott suggested that the strong electron-electron interaction splits the $3d_{\|}$ band and generates the gap [14]. They stated that pairing of the V atoms has little effect on the gap and emphasized the importance of the correlation energy U_c [14]. They approximated the energy gap to be U_c - ½B_1 where B_1 is the width of the $3d_{\pi}^{*}$ band [14]. Later on, Paquet & Leroux-Hugon build up a band model for VO_2 which started from the tight-binding approximation and included both Mott-Hubbard and Peierls mechanisms [33]. They concluded that electron correlations are the driving mechanism stabilizing the monoclinic distorted phase which, in turn, is a consequence of this primary mechanism [33].

The importance of the band structure to MIT characteristics has been experimentally verified. Ruzmetov *et al.* pointed out that the $3d_{\|}$ band has an important role in the appearance of MIT in VO_2 using X-ray absorption spectroscopy (XAS). They reported that there exists a clear correlation between the increase of the spectral weight of the $3d_{\pi}^{*}$ band and the strength of MIT. The changes of the $3d_{\pi}^{*}$ band was attributed to it being overlapped with the $3d_{\|}$ band which strengthens due to electron-electron correlation. [34]

3.2.4. Effect of Strain in VO_2

The transition temperature T_{MIT} has been observed to be pressure-dependent suggesting that stress caused by strain in thin films might have the same effect [35, 36]. The strain is induced by the lattice mismatch between the film and the substrate as discussed earlier in Chapter 2.4. Therefore, the substrate would have an important role in MIT characteristics by affecting the strain state of the film [7]. Especially, the uniaxial stress along the *c*-axis of the tetragonal R phase, *i.e.* c_R-axis, has been acknowledged to significantly influence the transition temperature [32, 36, 37]. Because MIT is accompanied by the structural phase transition where the lattice constants are remarkably changed, it is expected that a uniaxial compressive stress along the c_R-axis drives the system towards the metallic phase whereas the insulating phase is induced by tensile stress [37]. The magnitude of the transition temperature change caused by uniaxial stress σ is predicted by Clausius–Clapeyron equation

$$\frac{dT_{MIT}}{d\sigma} = \frac{\varepsilon T_{MIT}^{0}}{\Delta H}, \tag{17}$$

where ε is the strain and ΔH is the latent heat of the transition [37]. According to the equation, the transition temperature is more susceptible to uniaxial stress than to hydrostatic pressure because the change of length along the c_R-axis is stronger than the change in the volume at MIT [37].

Muraoka & Hiroi studied epitaxial VO_2 films with thickness 10 - 15 nm grown on TiO_2 (001) and (110) substrates. They expected the c_R-axis length to decrease in the VO_2 (001) thin films grown on TiO_2 (001) due to in-plane tensile stress whereas the epitaxial stress in the VO_2 (110) films on TiO_2 (110) should cause the c_R-axis length to increase. This was confirmed by XRD measurements which were performed above the transition temperature. The measured hysteresis curves revealed that the transition temperature in the film on TiO_2 (001) was reduced to 27 °C, while it was increased to 96 °C in the film on TiO_2 (110) compared to the value of 68 °C reported in single crystal, suggesting that shorter c_R-axis length results in lower T_{MIT}. Since the c_R-axis length expresses the distance between adjacent vanadium atoms, it was concluded that the reduced c_R results in direct overlapping of the 3*d* orbitals, thus increasing the width of the 3*d* band and stabilizing the metallic phase. [36]

Similar results have been provided by Aetukuri *et al.* who modified the epitaxial strain by varying the thickness of a RuO_2 buffer layer which was deposited between the VO_2 thin film and the TiO_2 substrate. Once again the VO_2 (001) film was tensile-strained on bare TiO_2 (001), but it was compressively strained in-plane when deposited on relaxed RuO_2 (001). Indeed, the rutile VO_2 (002) diffraction peak from the films, each 30 nm thick, was observed to monotonically shift to lower angles with increasing buffer layer thickness, which is an indicative of increasing out-of-plane lattice constant, *i.e.* c_R-axis length. The lowest transition temperature of 12 °C was measured in the mostly strained film which was deposited on 10 nm thick RuO_2 layer, and the temperature was observed to increase up to 72 °C with increasing buffer layer thickness. On the basis of XAS measurements, this effect was related to the strain-dependent changes of the *p*-*d* hybridization which modifies the orbital occupation in the metallic phase. The orbital occupation of the $3d_{\pi}^{*}$ orbitals was explained to increase while the orbital occupation of the $3d_{||}$ orbitals decreases because the $3d_{\pi}^{*}$ band is lowered relative to the $3d_{||}$ band when c_R is decreased. It was concluded that the transition temperature is more influenced by orbital-lattice coupling than the electron-electron correlation energy U_c when Mott transition is bandwidth controlled rather than filling controlled. [32]

Vanadium dioxide has also been synthesized in other forms than thin films such as nanoparticles, nanobeams, and microcrystals [37 - 43]. Because of the size effects which are present in these nanostructured forms of VO_2, the metal (M) and insulator (I) domains have distinct light scattering properties allowing one to investigate the actual variation of these domains during MIT by optical microscopy [37 - 39]. Wu *et al.* studied the substrate-induced strain in VO_2 nanobeams and observed that the interaction between the substrate and the beam, which results in uniaxial strain in the nanobeam, changes the relative thermodynamic stability of the M and I phases [39]. Similar study has been presented by Cao *et al.* but also with free-standing nanobeams which eliminates the substrate-induced strain and allows one to observe the strain effect solely by applying external stress [37]. By applying compressive strain of

about 2.1 % along the beam length, which was directed along the c_R-axis, the authors demonstrated for the first time that MIT in VO_2 can occur at room temperature [37].

To interpret the electrical behavior of VO_2 near the transition temperature more precisely, it is necessary to distinct the insulating phases since both M_1 and M_2 phases can coexist and have a clear impact on the measured resistivity curve [40, 41]. The identification of the phases and the investigation of the changes in their organization have been realized by temperature-dependent measurements using Raman spectroscopy and X-ray diffraction [40 - 43]. It has been observed that M_2 phase appears in between the transition from pure M_1 to pure R phase, and that all the three phases can also coexist at some point [40 - 43]. However, VO_2 initially in M_2 phase is found to directly transform into R phase [43]. Sohn *et al.* analyzed the fractional variation of the phases which revealed that the variation of M_1 and R phases across MIT shows a typical hysteresis behavior as in electrical hysteresis loops [41]. On the other hand, the variation of M_2 phase showed divergent behavior since the phase was rather an intermediate state which affected the distribution of M_1 and R phases [41].

The appearance of M_2 phase has been related to the tensile stress at M_1/R phase boundary which stabilizes M_2 phase because of its larger lattice constant along the c_R-axis compared to that of M_1 phase [40, 42, 43]. Compressive stress, on the other hand, favors the formation of M_1 and R phases because of their shorter lattice constant along the c_R-axis [43]. The stabilization of M_2 phase is clearly attributed to stress since VO_2 nanobeams are observed to undergo direct R to M_1 phase transition upon cooling after relaxation at high temperatures which resulted in compressive strain [40]. Furthermore, VO_2 initially in M_2 phase at room temperature is found to relax into M_1 phase when it is released from the substrate as observed in microcrystals [43]. Cao *et al.* have mapped the stress-temperature phase diagram of VO_2 over a large range of strain illustrating the stress/strain and temperature dependency of the phase transition [44].

4. X-RAY DIFFRACTION

4.1. Generation of X-Rays

A lot of information can be gained by studying the interaction between material and electromagnetic radiation. X-rays are particularly a powerful way to gain insight to the inner structure of matter because the wavelengths of X-rays are in the same scale as the interatomic distances. For this reason, constructive and destructive interference occurs between X-rays that are scattered from atoms. In the case of a constructive interference, the scattered waves are said to diffract. The observable diffraction depends on the phase difference between the scattered waves which, in turn, is related to the atomic distances. Therefore, X-ray diffraction can be utilized, especially, in structural analysis of crystalline material since there is a definite relation on how the atoms are arranged in a crystal. In addition, X-ray inspection is nondestructive so the material under investigation isn't affected during or after the process.

Synchrotron radiation and fluorescent X-ray emission are the main processes for generation of X-rays. Synchrotron radiation emerges from the acceleration and deceleration of charged particles, such as electrons, when they travel through magnetic fields. Synchrotron radiation requires large facilities but produces radiation from a broad range of spectrum with high intensity. Characteristic X-rays, on the other hand, are generated when electrons make transitions to lower energy states in an atom. This results in an emission of photon with energy that corresponds to the energy difference ΔE between the energy states. The relationship between photon energy, frequency f, and wavelength λ is given in equation (18).

$$\Delta E = hf = \frac{hc}{\lambda}, \tag{18}$$

where h is the Planck constant and c is the velocity of light. For an electron to occupy this lower state, there, however, must be an unfilled state called vacancy. Otherwise the transition cannot occur because of the Pauli exclusion principle. Vacancy can be generated by bombardment of photons or particles which have high enough energy to remove an electron from that shell. To produce characteristic X-rays, electrons must be expelled from the innermost energy states requiring more energy.

In an X-ray tube, which serves as a source for X-rays, electron bombardment is utilized in a high vacuum environment. The electrons are produced by heating a cathode filament made of metal and then accelerated in high voltage towards the anode. The produced X-rays will then be characteristic to the anode material. Typical anode materials are metals, such as copper or molybdenum. The intensities of the produced radiation depend on the probabilities of their respective electron transitions. For this reason, Kα radiation is mostly used since the produced intensity is higher than that of the Kβ radiation.

4.2. X-Ray Scattering

X-rays can be elastically or inelastically scattered by an electron. In inelastic scattering process, known as Compton scattering, the X-ray photon loses some or all of its energy to the electron. Elastically scattered X-rays, on the other hand, will conserve their energy and coherency. This process is named Thomson scattering, and it paves the way for structural characterization of materials. The importance of Thomson scattering lies in coherency of the scattered waves; if the phase relationship of the incident and scattered waves would be lost, the interference would not be observable.

Scattering is related to the interaction of the electromagnetic wave with the electron. The varying electric field of an X-ray will exert force on the electron causing the electron to oscillate, *i.e.* accelerate and decelerate during its motion, and therefore to emit an electromagnetic wave [45]. X-rays are also scattered by the nuclei but the intensity is so much less that it can be neglected [5].

In the kinematical scattering theory, it is assumed that the interaction between the X-ray and crystal is weak because the beam is considered to scatter only once which leads to more simplified treatment of the phenomenon. This assumption is, however, no longer valid for macroscopic perfect crystals in which case the multiple scattering effects become important. This is dealt within the dynamical scattering theory. [46]

Electrons are the most elementary scattering units and their ability to scatter X-rays is expressed in terms of a scattering length. For a free electron, it is of the form

$$r_0 = \frac{q_e^2}{4\pi\varepsilon_0 m_e c^2}, \tag{19}$$

where q_e is the elementary charge, ε_0 is the vacuum permittivity, m_e is the mass of electron, and c is the velocity of light. This is known as Thomson scattering length, and it is the classical radius of an electron. [46]

For electrons in atoms, the fact that they have finite spatial extent has to be considered. Electrons are now described as a charge distribution $\rho(r)$, and the scattered radiation is superposition of the scattered field by individual electrons. The total scattering length of an atom can therefore be presented as

$$-r_0 f^0(Q) = -r_0 \int \rho(r) e^{iQ\cdot r}\, dr, \tag{20}$$

where the factor $f^0(Q)$, known as the atomic form factor, is a Fourier transform of the electronic charge distribution. It represents the atomic scattering amplitude, and it can be evaluated from the quantum mechanical description of electrons. The scattered intensity is proportional to the square of the total scattering length. [46]

The exponential term in equation (20) is a phase factor which represents the phase difference between waves scattered from the origin and from point r. Scattering from an atom is illustrated in Figure 5, which has been modified from Als-Nielsen & McMorrow. [46]

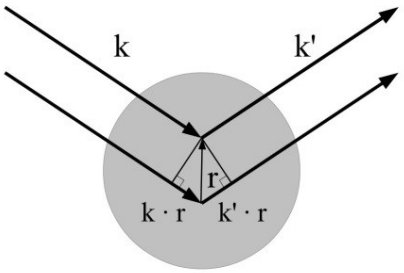

Figure 5. Scattering from one atom.

The argument Q in equation (20) is the scattering vector defined as

$$Q = k - k', \tag{21}$$

where k and k' are the wave vectors of the incident and scattered wave, respectively. In case of elastic scattering, the wave vectors are equal, *i.e.*

$$|k| = |k'| = \frac{2\pi}{\lambda}, \tag{22}$$

so the magnitude of the scattering vector is

$$|Q| = 2|k|\sin\theta = \frac{4\pi}{\lambda}\sin\theta, \tag{23}$$

where θ is the incident angle which is equal to the exit angle. The relation between the scattering vector Q and wave vectors k and k' can be depicted by means of the scattering triangle. Scattering triangle for elastic scattering process is shown in Figure 6, which has been modified from Als-Nielsen & McMorrow. [46]

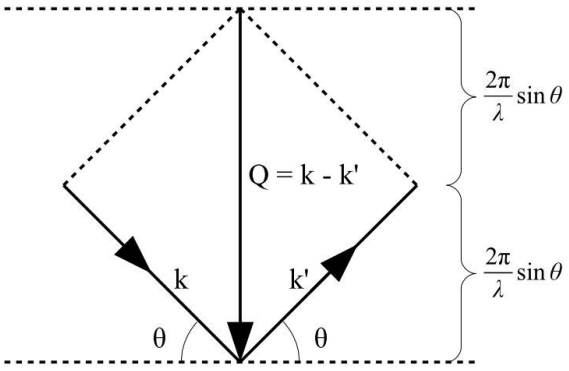

Figure 6. Scattering triangle for elastic scattering event.

The scattering vector can vary in between 0 and infinity, so that the corresponding value of the atomic form factor can have values in between

$$f^0(Q) = \begin{cases} Z & \text{for } Q \to 0 \\ 0 & \text{for } Q \to \infty \end{cases}, \tag{24}$$

where Z is the number of electrons in an atom. The explanation for this behavior is that when the scattering vector is zero, *i.e.* scattering in forward direction, the phase factor approaches unity and there is no phase difference between the scattered waves.

Therefore, it is a contribution of all the waves scattered from all the electrons in an atom. On the other hand, when the scattering vector increases and the wavelength becomes small compared to the atom, electrons start to scatter out of phase and the waves then interfere destructively leading to a damping of the diffraction pattern. While Thomson scattering tends to decrease with high Q, the inelastic and incoherent Compton scattering is increased at the same time. [46]

In a crystal, the scattering is related to the atomic content which, in turn, is related to the scattering from the electrons in an atom. For a crystalline material, the position of any atom can be presented as

$$r_l = R_n + r_j , \tag{25}$$

where R_n is the lattice vector and r_j defines the positions of atoms in unit cell. The scattering amplitude can now be presented as a Fourier transform of the crystal structure which decomposes into the product of two terms as presented in equation (26).

$$F(Q) = \sum_{R_n + r} f_j(Q) e^{iQ\cdot(R_n + r_j)} = \sum_n e^{iQ\cdot R_n} \sum_j f_j(Q) e^{iQ\cdot r_j} , \tag{26}$$

where the first term is a sum over the lattice and the second term is a sum over the basis of atoms having a form factor $f_j(Q)$. The latter is known as the unit cell structure factor. [46]

The terms in the lattice sum are phase factors, and if

$$Q \cdot R_n = m2\pi , \tag{27}$$

where m is an integer, is fulfilled, the sum becomes of order N_u, which is the number of unit cells, because all the phases of the scattered waves will add up coherently thus producing an intense signal. Otherwise the term will be of order of unity and the scattered intensity vanishes due to destructive interference. [46]

Since the scalar product of the lattice vectors in reciprocal and direct space is

$$G_{hkl} \cdot R_n = 2\pi(hn_1 + kn_2 + ln_3) = m2\pi , \tag{28}$$

a unique solution to equation (27) is of the form

$$Q = G_{hkl} , \tag{29}$$

which is Laue condition for the observation of diffraction from a crystal. It states that diffraction occurs only if the scattering vector coincides with the reciprocal lattice vector. Thus the scattering from a crystal is confined to distinct points in reciprocal space, and the intensity in each point is modulated by the absolute square of unit cell structure factor. [46]

The unit cell structure factor in equation (26) can now be presented as

$$F_{hkl} = f(G) \sum_j e^{iG\cdot r_j} , \tag{30}$$

where it has been assumed that the all atoms in the unit cell are identical [46]. The summation can be calculated for Bravais lattices revealing that some reflections from planes (*hkl*) are forbidden since they yield a zero coefficient. These reflections, although predicted by Bragg's law, are thereby not observed. Bragg's law is the general form of Laue condition, and it is presented as

$$2d_{hkl}\sin\theta_B = m\lambda, \tag{31}$$

where θ_B is known as Bragg angle, which gives the maximum intensity, and *m* is a positive integer, which represents the order of diffraction. Bragg reflections from the same plane (*hkl*) but with different order are usually termed *m*(*hkl*). Geometrical representation of Bragg's law is shown in Figure 7.

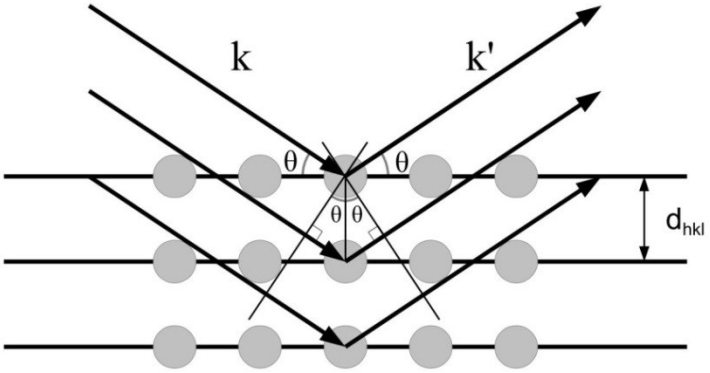

Figure 7. Geometrical representation of Bragg's law.

4.3. X-Ray Diffraction Measurements

4.3.1. θ-2θ Scan

In X-ray diffraction, Bragg reflections are of interest because the positions, shapes, and intensities of the measured peaks are related to the microstructure of the material. An instrument which is often used to measure Bragg reflections of a thin film is the θ-2θ diffractometer. Because the scattered intensity depends on the distance from the sample to the detection system, the distance has to be kept constant during the measurement. The movement of the detector is therefore restricted to a sphere of constant radius with the sample positioned in the center of it. Since the wave vectors *k* and *k'*, and the surface normal form a common plane, called scattering plane, the geometry is said to be coplanar. [5]

The symmetric θ-2θ scan is the mostly used technique to acquire diffracted signal. The X-rays impinge the sample at an angle θ while the detector monitors the scattered radiation at the same angle. The angle between elongation of the incoming beam and the exiting beam is thus 2θ. During the scan, the angle is varied to measure intensities from an angle 2θ but the incident and exit angle are kept equal. Therefore, the scattering vector will always be parallel to the surface normal, and Bragg reflections occur only from the planes (*hkl*) which are parallel to the surface plane of the sample. Because of the finite divergence of the beam, the scattering vector is, however, somewhat tilted from the surface normal for the beams which deviate from the central beam. This causes reflections also from the planes which are not quite parallel to the surface plane. [5]

The measurement geometry of the symmetric θ-2θ scan is shown in Figure 8. The figure has been modified from Birkholz [5].

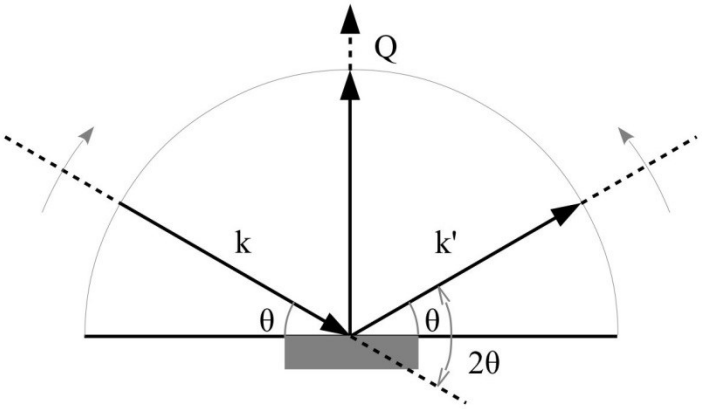

Figure 8. Measurement geometry of the symmetric θ-2θ scan.

The intensity of X-ray is reduced as they transit through matter because of absorption. The exponential attenuation of the intensity is given by Lambert-Beer law

$$I(l_t) = I_0 e^{-2\mu l_t}, \tag{32}$$

where I_0 is the intensity of the incoming radiation, μ is the linear attenuation coefficient, and l_t is the path length. The parameter μ depends on the wavelength of the X-ray, as well as on the chemical composition and density of the sample. Its inverse

$$\tau_{1/e} = \frac{1}{\mu} \tag{33}$$

specifies the penetration depth $\tau_{1/e}$ along the surface normal for which the intensity has decreased to value of 1/e (37 %) of its initial value. For Cu Kα radiation, the penetration depths for many materials vary from 0.1 to 10 μm, which corresponds to typical layer thicknesses. The effect of absorption then reduces the scattered intensity, which is a special feature in thin film analysis. In addition, since the X-ray beam can penetrate the thin film, the diffraction pattern is also influenced by the reflections from the underlying substrate. [5]

Absorption factor A, also known as the thickness factor, is used to describe the reduced intensity in a thin film sample with thickness t_f compared to an infinite thick sample. Since the relation of the path length and thickness can be expressed as

$$l_t = \frac{t_f}{\sin\theta}, \tag{34}$$

the absorption factor for the θ-2θ geometry is

$$A_{\theta-2\theta} = \left(1 - e^{\left(-\frac{2\mu t_f}{\sin\theta}\right)}\right), \tag{35}$$

where the dependence on the thickness of the film and linear absorption coefficient is known as the μt_f product. It can be seen that the measured intensity of Bragg reflection scales down with increasing scattering angle. The decrease is due to the fact that when the angle 2θ is increased, the irradiated volume becomes smaller. [5]

4.3.2. Grazing Incidence X-Ray Diffraction

In the case of thin films, the penetration depth of X-rays mostly exceeds the thickness of the film. This causes a large fraction of the intensity to reflect from the substrate rather than the film itself when θ-2θ configuration is utilized. The path travelled by X-ray in the sample can be significantly increased by utilizing small angles of incident. This technique is known as the grazing incidence X-ray diffraction (GIXRD), and it makes it possible to obtain depth-resolved structural information by probing the sample under different angles of incidence. [5]

The incident angle, denoted by α_i, is usually only few degrees or even less. During the measurement, it is kept constant while the detector is moved along the 2θ circle so that the angle between the sample surface and outgoing beam is $2\theta - \alpha_i$. This distinguishes GIXRD from the symmetric θ-2θ configuration but both are coplanar configurations. The intensity is similarly gathered from the angle 2θ and Bragg peaks are found at comparable positions. [5]

The difference in the measurement geometry of symmetric and asymmetric scan has a clear impact on the orientation of the scattering vector. In grazing incidence configuration, the orientation of the scattering vector changes in the course of the measurement, and it is not parallel to the surface normal. Since the orientation of the scattering vector is constantly changed, the measurement probes planes which are tilted with respect to the sample surface and which are not parallel to each other. The change in the orientation of the scattering vector with respect to the surface normal is

$$\Omega = \alpha_i - \frac{2\theta}{2}, \tag{36}$$

where α_i is the incident angle and 2θ is the angle between elongation of the incident beam and the exit beam. [5]

The measurement geometry of GIXRD method is shown in Figure 9. The figure has been modified from Birkholz [5].

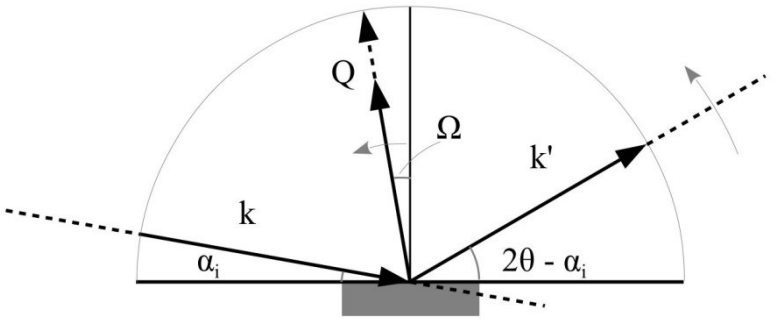

Figure 9. Measurement geometry of the asymmetric scan.

Since the beam course is different in GIXRD, the absorption factor has to be modified by a factor

$$k_\alpha = \frac{1}{\sin\alpha_i} + \frac{1}{\sin(2\theta - \alpha_i)} \tag{37}$$

so that

$$A_\alpha = \left(1 - e^{-\mu t_f k_\alpha}\right). \tag{38}$$

Equation (38) is valid for any measurement configuration and consequently corresponds to equation (35) in the case of θ-2θ scan. Since the configuration factors differ for the θ-2θ and 2θ scans, the absorption factors also behave differently. In case of asymmetric scan, the intensity is not decreased with increasing 2θ angle but stays rather constant. [5]

4.3.3. Reciprocal Space Mapping

In coplanar configurations, the scattering vector can vary in z and x directions. The z direction denotes the direction of the surface normal whereas the x direction is in the plane of the sample. In the case of symmetric scan, only the out-of-plane component Q_z is altered during the measurement. During the asymmetric scan, however, the scattering vector has also the in-plane component Q_x excluding the case when the incident and the exit angle are equal, *i.e.* $\alpha_i = 2\theta/2$. Utilizing the z and x components of the scattering vector, the different scanning techniques and the condition for diffraction can be visualized in the plane of scattering vector. [5]

For this purpose, the angular coordinates of the measurement setup in direct space are converted into coordinates of the scattering vector Q using equations (39) and (40) [6].

$$Q_x = k(\cos(\alpha_f) - \cos(\alpha_i)) = k(\cos(2\theta - \alpha_i) - \cos(\alpha_i)), \tag{39}$$

$$Q_z = k(\sin(\alpha_i) + \sin(\alpha_f)) = k(\sin(\alpha_i) + \sin(2\theta - \alpha_i)), \tag{40}$$

where k is the magnitude of X-ray wave vector, α_i is the incident angle, and α_f is the exit angle [6]. On the goniometer, the incident and exit angle relate to the rotation of the sample, denoted by ω, and the detector, denoted by 2θ, so that $\omega = \alpha_i$ and $2\theta = \alpha_i + \alpha_f$ when utilizing different scans to collect reciprocal space maps (RSM) [6]. Depending on the diffractometer, the rotation of the sample by Δω can be performed physically or by respectively moving the X-ray source and the detector.

The Q space from which diffraction data can be obtained is restricted to a hemisphere so that Q_x can have values in between $-2k$ and $2k$, while Q_z is confined in values between zero and $2k$. In addition, the area is divided by two other hemispheres of radius k centered in Q_x at positions $-k$ and k. These correspond to regions which are accessible only by transmission geometry. The representation can be completed by combining it with a reciprocal map of the sample to illustrate the conditions for diffraction. Reciprocal space maps are obtained by mapping the area in the vicinity of Bragg reflection under investigation. The area is mapped by performing various one-dimensional scans which are then joined together in Q space. [5]

Figure 10 and Figure 11 show illustrations of two different scanning techniques in reciprocal space. The light blue area in the hemisphere, which is restricted by two grey semicircles, defines the region in reciprocal space which can be accessed by the diffractometer when using Cu Kα radiation. The spots mark the positions of Bragg reflections from a *c*-plane sapphire so the spots along the surface normal where $Q_x = 0$ are reflections from (000*l*) planes. The blue lines near the (0006) reflection represent the reciprocal area which is scanned during the measurement.

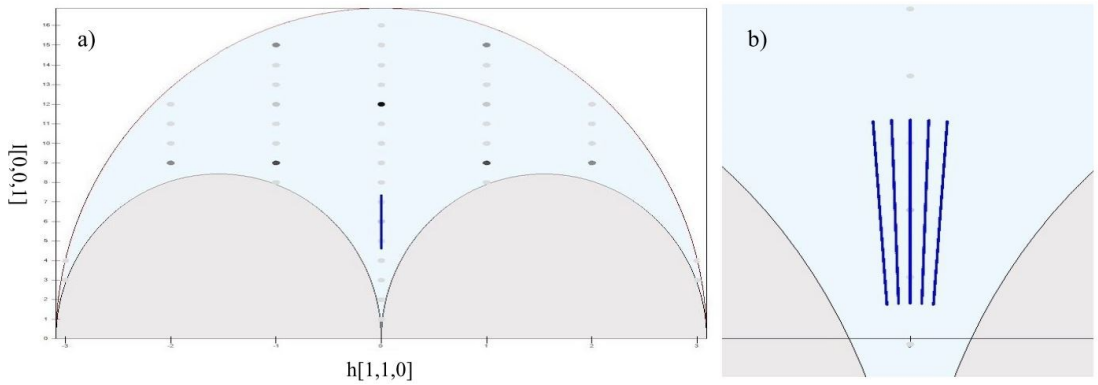

Figure 10. Reciprocal representation of symmetric scan.

The blue line in Figure 10a) illustrates the behavior of the scattering vector during symmetric θ-2θ scan. This method is known as the specular or Q_z scan since the measurement proceeds along the Q_z direction parallel to the surface normal during which the incident and exit angle are kept equal [6]. Figure 10b) shows how information can be obtained from a larger area by performing subsequent scans which are afterwards combined together to form a reciprocal space map. Between the scans, the sample is rotated by Δω, and the measurement proceeds as before by rotating the source and the detector by the same amount to scan the whole 2θ range. The method is known as radial or offset scan of which the specular scan (centermost line) is a particular case [6]. The scan is now, however, directed inclined to Q_z as ω differs from 2θ/2 [6].

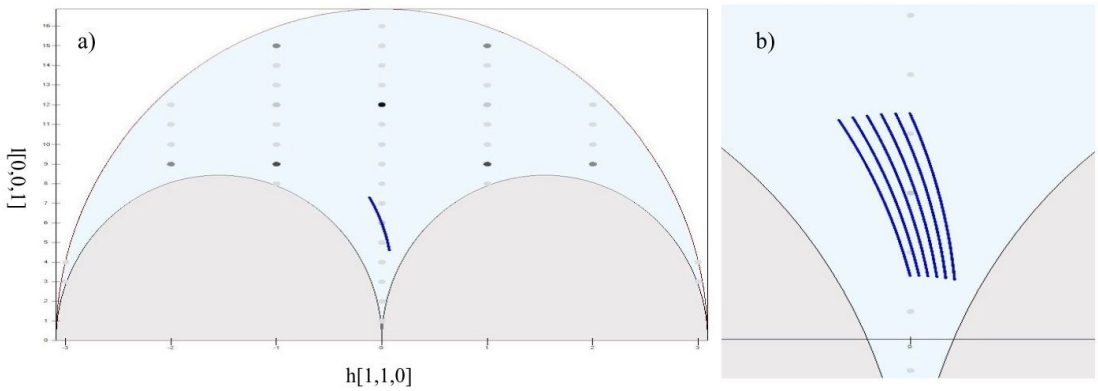

Figure 11. Reciprocal representation of asymmetric scan.

Figure 11 presents an example of how the asymmetric scan can be utilized to collect reciprocal space maps. The method shown in Figure 11a) is known as the α_f, detector, or 2θ scan since only the detector is moved during the scan drawing a circumference of a circle within the Q plane [6]. In Figure 11b), a more comprehensive area is recorded by subsequent 2θ scans. Rotating the sample by Δω between the scans, information from the circumference of different origin in Q space is collected.

4.3.4. Line Profile Analysis

Line profile analysis (LPA) is used to derive microstructural information from measured Bragg peaks. The analysis is based on numerical regression of the measured peaks using standardized model functions from which parameters such as peak position and intensity, as well as parameters related to the shape and width of the peak can be obtained. Cauchy and Gauss functions are the prototype model functions in LPA because their profile is associated to the size broadening and strain broadening, respectively. This stems from the fact that the Kα radiation of an X-ray tube is naturally Cauchy shaped and the deviation of interplanar spacings is often normally distributed around the average d_{hkl} value. However, since pure Cauchy or Gauss profile rarely matches to the shape of the measured peak, other mathematical functions, which are based on the combination of both two, are also used. [5]

Crystallite size and strain are typical microstructural properties that are present in thin film samples causing broadening of Bragg peaks. When the crystallite size decreases, the width of Bragg reflection increases which makes it possible to derive the crystallite size from the peak profile. The obtained crystallite size corresponds to the size of the domains which scatter the incoming X-rays coherently. These domain sizes are generally smaller than the crystallite size obtained by other techniques such as transmission electron microscopy. [5]

Besides size broadening, the width of Bragg peaks is affected by any distortion of the crystal structure such as microstrain, dislocations, and stacking faults of which microstrain and dislocations play a major role. Strain can be classified into microstrain and macrostrain depending on the length scale they appear in. Strain fields appearing on a length scale smaller than the inverse linear attenuation coefficient of the X-ray beam are denoted as microstrain contrary to macrostrain which exceeds the value. These strains affect Bragg peak through the variation of the interplanar spacings d_{hkl}. Because of microstrain, the interplanar spacing has certain distribution rather than a specific value which causes broadening of the peak. Macrostrains, on the other hand, cause a complete shift of the peak. [5]

5. THIN FILM DEPOSITION

5.1. Thin Film Growth

The film begins to form when the bare substrate is exposed to vapor atoms or molecules which then condense on the surface. In the early stages of film formation, the film is observed to grow in three basic growth modes. One of the modes is called island or Volmer-Weber growth, which occurs when the deposited atoms or molecules more likely bind to each other than to the substrate. After the smallest stable clusters have nucleated on the substrate, they start to grow in three dimensions and form islands. Other mode is called layer or Frank-Van der Merwe growth. Now the clusters rather grow in two-dimensions forming planar sheets because the atoms are more strongly bound to the substrate than to each other. After the first monolayer has formed, a second layer, which is somewhat less tightly bound, will begin to build up. The third growth mode, called Stranski-Krastanov growth, is quite common, and it combines the island and layer growth. The film formation begins with the layer growth, but it becomes unfavorable after the completion of first layers so the growth proceeds with the island growth. [47]

5.2. Pulsed Laser Deposition

Pulsed laser deposition (PLD) is a physical vapor deposition method which utilizes a high energy laser beam and a vacuum chamber to deposit thin films. The deposition can be carried out in a plain vacuum environment or in the presence of background gas. Oxygen is commonly used as a background gas to deposit oxides whose stoichiometry is controlled by the gas pressure. The deposition is based on the interaction of the laser beam with the target material. The target material, which is placed inside the chamber, is ablated and evaporated when the external laser is focused onto its surface using lenses [47]. The laser is usually a gas laser operating in the ultraviolet range of the optical spectrum because ultraviolet light is strongly absorbed by most nonmetallic materials [47]. The lenses and window materials have to be transparent to the used laser wavelength [47]. Such material is quartz glass in the case of ultraviolet lasers, for example [47].

The amount of absorption depends on the laser wavelength, and it usually increases with decreasing wavelength, *i.e.* increasing photon energy [47]. Strong absorption results in reduced penetration depth so the interaction takes place on the surface of the target material [47]. Induced by thermal, chemical, and mechanical reactions, the absorbed energy causes ablation, excitation of atoms, and formation of plasma in the target surface [47]. A highly directional plume of evaporated species is then ejected from the target towards the substrate where they condense and form a film [47]. The plume contains energetic atoms, ions, clusters, and molten droplets, among others [47]. In the presence of a background gas, the ablated species interact with the gas molecules [48]. To allow evaporation, ablation, and other reactions, the laser beam fluence (J/cm^2) must exceed certain threshold value for the given target material [47]. The fluence can be adjusted by changing the energy and spot size of the laser beam.

One of the drawbacks of PLD is the possible generation of particulates which are incorporated into the film [47]. One solution to overcome this nuisance is to use a

spinning mechanical shutter between the target and the substrate allowing the more mobile species to pass through while filtering the slower, larger particulates [47]. Other drawback results from the highly directional plume which prevents the film to be uniformly deposited over large areas [47]. This can be somewhat influenced by rotating the substrate and changing the hitting location of the laser beam on the target during deposition. The target can also be rotated allowing more uniform wear of the target. By utilizing multiple targets, it is possible to manufacture layered films of different elements [47]. The targets can be sequentially ablated by deploying several lasers or using a single laser and beam splitters [47]. Single laser alone can be utilized when the targets are mounted on a rotating carousel [47].

PLD method has many advantages. For example, the chemical composition and stoichiometry of complex oxide targets can be easily repeated in the film, the film adhesion is excellent, and the microstructure can be controlled from amorphous to single crystalline films. The method also allows deposition of materials with very high melting points and fabrication of compounds with phases which would otherwise be metastable.

The deposition is usually carried out at high temperatures by heating the substrate up to several hundreds of Celsius degrees. High temperature results in increased mobility of the atoms on the surface of the substrate during growth [49]. In the case of vanadium dioxide, the film grows in the metallic R phase when the substrate is heated above the phase transition temperature. The deposition can also be carried out in room temperature followed by post-annealing process. In post-annealing, the manufactured film-substrate system is heated and cooled after the deposition in the presence of background gas. Vanadium dioxide thin films have been successfully grown using both procedures. Nag *et al.* have reported that post-annealing produces VO_2 thin films with higher quality and better MIT characteristics than direct high-temperature growth [49]. It was speculated that the high-temperature growth induces more strain to the film which, for example, leads to increased surface roughening which results from the strain relaxation generating misfit dislocations [49].

6. OTHER EXPERIMENTAL METHODS

6.1. Raman Spectroscopy

Raman spectroscopy investigates elementary excitations such as phonons [3, 4]. It can be utilized in material analysis since it provides a way to identify chemical phases and crystal symmetries. It is an optical method which has its basis on the scattering of photons when the sample is illuminated. This interaction between the light and the material is related to the polarizability of the valence electrons [3, 4]. The scattering involves an excitation of atoms or molecules to a higher energy state followed by a relaxation to a lower energy state. If the atom or molecule returns to the same state as before the absorption, the energy of the scattered photon will be the same as the energy of the incoming photon. This elastic interaction is known as Rayleigh scattering. The photons can also scatter inelastically involving a change in their energy. This process, which is known as Raman scattering, is much less likely to occur. Inelastic scattering of X-rays is identical to this process [3]. By analyzing the frequency of inelastically scattered photons, the material under investigation can be identified because the frequency shift is related to the characteristic energy states of the material. Raman modes which are present in the spectrum result from the excitations which are allowed by specific selection rules [3, 4].

Raman spectrum of the metallic phase of VO_2 is featured by a strong fluorescence background with some broad Raman peaks, for example, at 240, 390, and 510 cm^{-1} [50, 51]. Eighteen Raman-active modes are present in both M_1 and M_2 phases [52]. M_1 phase exhibits peaks at around 190, 220, 260, 310, 340, 390, 500, and 610 cm^{-1}, for example [40, 42, 43, 52]. Raman spectrum of M_2 phase includes peaks at 200, 230, 270, 300, 340, 440, and 650 cm^{-1} [40, 42, 43, 52]. Upon the transformation from M_1 to M_2 phase, the noticeable changes in Raman spectrum include the shifts of the 190 and 610 cm^{-1} M_1 modes to higher frequencies [40, 42, 43]. However, the coexistence of the phases is hard to verify due to the similarities in Raman modes. A peak around 625 cm^{-1}, for example, can be a contribution of both 610 cm^{-1} (M_1) and 650 cm^{-1} (M_2) modes which can only be resolved by proper fitting [53].

6.2. Atomic Force Microscopy

Atomic force microscopy (AFM) is an example of the various scanning probe microscopy (SPM) techniques that are utilized in thin film research. Atomic force microscope can be used to characterize the morphology of a thin film and to form images of its surface. The operation is based on sensing the force exerted by the surface to a small tip of a cantilever. Based on the variation of the force, the surface can be imaged by scanning the tip across the surface. Because atomic force microscope detects force instead of current, as in the case of scanning tunneling microscope (STM) which is another type of SPM, AFM can be used to image all kinds of materials regardless of its conductivity [47]. The spatial resolution of STM is, however, better than that of the atomic force microscope [47]. To form an image of the film surface based on the mapped force, AFM instrument must include certain functionalities [47]. The instrument contains a mechanical system, which is usually piezoelectric, to raster scan the surface [47]. The cantilever deflection can be sensed

optically using a photodiode array or an interferometer [47]. The instrument also contains a feedback system which controls and monitors the force [47].

There are two basic modes of operation in AFM, namely the contact and non-contact AFM. In the former mode, the tip is in physical contact with the surface. As a consequence, the electron clouds of the tip and the film overlap, and the tip is pushed away due to repulsive electrostatic forces. In the latter mode, the tip is not in contact with the surface but is located one to tens of nanometers above it. Despite such separation, there still exist van der Waals forces which now cause a weak attraction between the tip and the film. To prevent surface contact, the used cantilever is stiff, and it is induced to vibrate so that small forces can be detected. Changes in the vibrational amplitude or in the resonant frequency are then related to the tip-surface spacings to provide an image of the surface. The non-contact mode of operation can be used to scan soft or elastic materials, and it reduces the tip degradation and surface contamination. [47]

6.3. Sputtering

Sputtering is a physical vapor deposition method which utilizes ion bombardment to deposit thin films. The ions are accelerated towards the target by means of electric or magnetic fields. The impact causes the target atoms to be ejected towards the grounded substrate facing the target where they begin to form a film. The substrate can also be biased which can influence the properties of the deposited film. In addition to the inert working gas, which is usually argon, a reactive gas, such as oxygen, can also be introduced into the deposition chamber in order to control the stoichiometry of the film. [47]

In this work, sputtering method was used to deposit electrodes on the thin films for the purpose of temperature-dependent resistance measurements. The sputtered material was platinum, and the thickness of the electrodes was about 220 nm.

6.4. Electrical Characterization

A Linkam TMS 94 heating stage and a Keithley 2612 source meter was used for the electrical characterization of the thin films, and they were controlled by a computer in a LabView environment. The temperature of the sample was changed from room temperature to 100 °C and back at the rate of 3 °C/min. The measurement voltage was kept constant at 100 mV during the temperature sweep, and by measuring the current, the resistance R could be calculated according to Ohm's law

$$R = \frac{U}{I}, \tag{41}$$

where U is the voltage and I is the current. The resistivity ρ of the film was then calculated using equation (42).

$$\rho = R\frac{w}{l_f}t_f, \tag{42}$$

where w is the width, l_f is the length, and t_f is the thickness of the film. The planar geometry of the thin film between the electrodes, *i.e.* the ratio w/l_f, was inspected by

an optical microscope, and the thickness of the film was evaluated by a Veeco Dektak 8 surface profiler.

7. RESULTS

7.1. Pulsed Laser Deposition of VO_2 Thin Films

Vanadium dioxide thin films were grown using PLD method on *c*- and *a*-plane Al_2O_3, *i.e.* sapphire, substrates. Prior to deposition, the substrates were ultrasonically cleaned in alcohol and blown dry with nitrogen gas. Pulses of ultraviolet light were generated from XeCl excimer laser operating at the wavelength of 308 nm. Duration of one pulse was 25 ns, and it ablated a ceramic V_2O_5 target with a 10 Hz pulse frequency. The distance between the substrate and the target was about 7.5 cm. The substrate was heated to the deposition temperature at the rate of 12.5 °C/min. The deposition was then carried out in a high vacuum environment after introducing oxygen into the chamber. After the deposition, the substrate was cooled down to near the ambient temperature at the rate of 5 °C/min under the same oxygen pressure. Other deposition parameters were optimized to obtain epitaxial growth of VO_2. The main parameters which were varied during PLD experiments were the oxygen pressure and the deposition temperature.

VO_2 thin films under investigation were grown under the same deposition conditions but with different number of pulses on *c*-plane sapphire. The laser beam fluence was set to 1.5 J/cm^2 and the oxygen partial pressure was kept at 2×10^{-3} mbar while the substrate temperature was fixed at 600 °C. The number of pulses ranged from 4000 to 60000. This provided seven VO_2 thin films with various thicknesses, namely 20, 30, 60, 100, 140, 200, and 240 nm. Based on the measured thicknesses, the deposition rate can be evaluated to be about 2.6 nm/min.

Thin films were also deposited on *a*-plane sapphire, and VO_2 was observed to epitaxially grow in both (010) and (100) orientations. Epitaxial (010) oriented VO_2 films were obtained with an oxygen partial pressure of 2×10^{-3} and 6×10^{-3} mbar when the substrate was heated to 600 and 650 °C, respectively. When the oxygen pressure was increased to 7×10^{-3} and 8×10^{-3} mbar, and the temperature was at 650 °C, epitaxial (100) oriented growth of VO_2 was observed. The fluence was set to 1.5 J/cm^2 in all the cases.

7.2. Structure and Lattice Parameters

XRD measurements were performed using Bruker D8 Discover diffractometer using Cu Kα radiation. The first measurements were conventional θ-2θ scans which were performed to analyze the structure of the deposited VO_2 thin films. Because the X-ray tube was observed to produce secondary radiation which was diffracted between the Kα and Kβ lines reflected from the substrate where the peaks from the film were, a β-filter made of nickel was inserted into the incident beam path. While the β-filter somewhat attenuates the Kα radiation, the peaks are a contribution of both $K\alpha_1$ and $K\alpha_2$ radiation generated in the X-ray tube. A knife edge was also adjusted right above the sample to reduce diffuse scattered intensity, which is more pronounced at lower scattering angles, from the background. XRD patterns measured from 2θ angle of 10 - 100° are presented in Figure 12 and Figure 13.

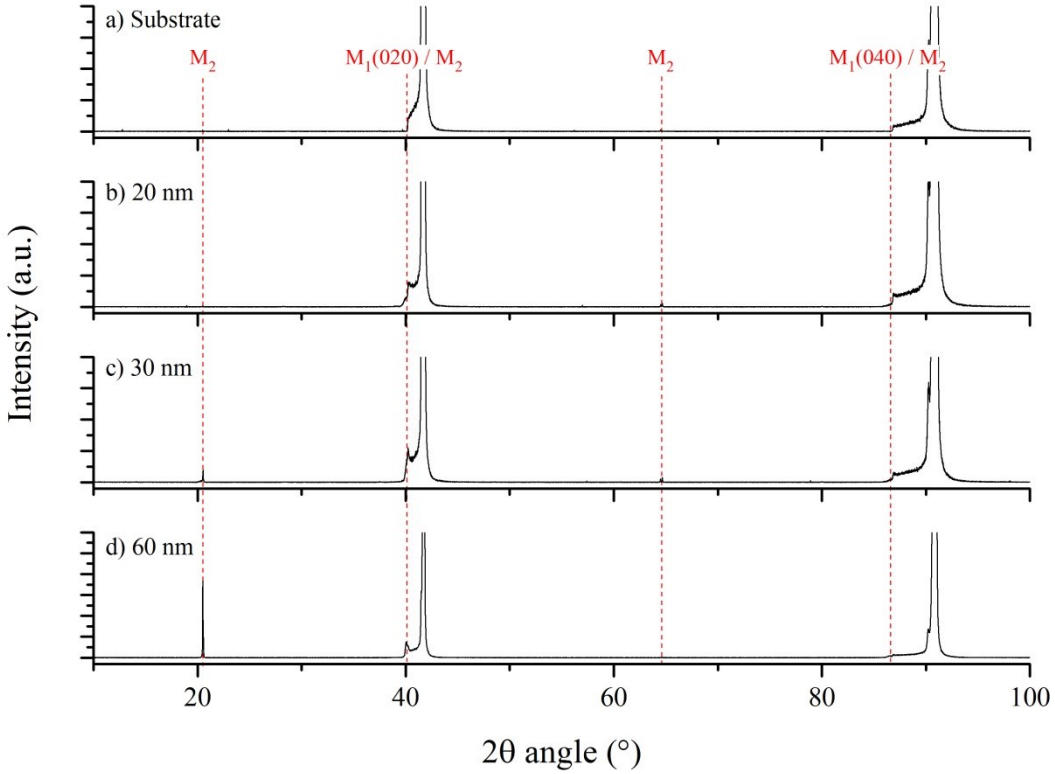

Figure 12. θ-2θ XRD patterns for the substrate and the three thinnest films. The vertical dashed lines mark the positions of M_1 and M_2 peaks.

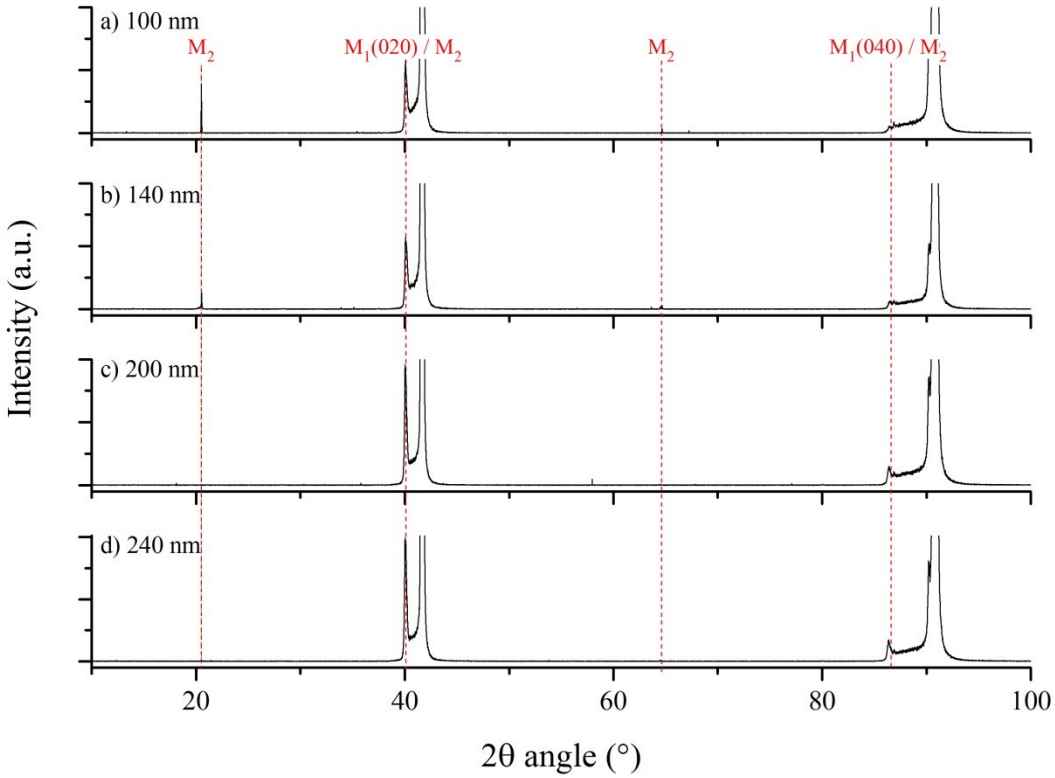

Figure 13. θ-2θ XRD patterns for the four thickest films. The vertical dashed lines mark the positions of M_1 and M_2 peaks.

Figure 12 shows XRD patterns for the three thinnest films. Also, the diffraction data of the plain *c*-plane sapphire substrate is presented for comparison. The most intense peaks at 41.7° and 90.8° are reflections from the Al_2O_3 (0006) and (00012) planes, respectively. The 2θ peaks at 40.0° and 86.4°, which are right on the absorption edge caused by the use of the β –filter, correspond to the (020) and (040) reflections from the monoclinic M_1 phase of vanadium dioxide, respectively. They can also be attributed to the another monoclinic phase of VO_2, namely M_2 phase. These two peaks are present in all of the films including the four thickest films whose XRD patterns are shown in Figure 13. Four of the films, which are 30 to 140 nm thick, show also a peak at 20.5° which is attributed to the monoclinic M_2 phase. One very weak peak at 64.65°, which is also attributed to M_2 phase, can be seen in some of the films. The positions of these M_2 peaks also correspond to the first- and third-order (0*k*0) reflections from M_1 phase, but they are forbidden by the structure factor. The (0003) and (0009) reflections from the substrate are also in the same range as the two M_2 peaks, but they are at slightly lower angle and their intensity was observed to be really small when using β-filter.

The conventional θ-2θ scan results indicate that M_1 phase has grown in (010) orientation on the *c*-sapphire substrate since reflections from other planes do not exist. The intensity of M_1 peaks is seen to increase with increasing film thickness as a result of the increased sample volume. Also, M_1 (040) peak is much less intense than M_1 (020) peak since the effective volume which is irradiated decreases significantly with increasing scattering angle. The intensity of M_2 peak at 20.5° is at maximum in the 60 nm thick film, and it systematically decreases when the film becomes thinner or thicker than 60 nm.

Although the presence of the absorption edge makes it harder to distinguish the exact peak positions at least in the case of the thinner films, a slight shift of M_1 peaks to lower scattering angles is still observable when the film thickness increases. The shift is more observable at higher scattering angles, *i.e.* for M_1 (040) reflection, which results from the behavior of the *sine* function in Bragg's law. The shift of the peaks to lower scattering angles indicates that the films are compressively strained out-of-plane. This means that the *b*-axis length of M_1 phase increases with the film thickness because the *b*-axis length is the same as the spacing between the (010) planes for the monoclinic unit cell. According to the *b*-axis length given in Table 3, M_1 (020) and (040) reflections would occur at 39.8° and 85.7°, respectively.

To derive more accurate structural information from the films, high-resolution XRD scans were performed on all the samples in the vicinity of M_1 (020) reflection. For this purpose, a 4-bounce monochromator that selects $K\alpha_1$ radiation was used in the beam path. While the use of a monochromator improves the resolution, the measurement time must be increased because the diffracted intensity is greatly reduced at the same time. After the measurements, the peaks were fitted with Origin software using Pearson IV profile function because it was observed to be best suited for all the peaks. The background was set to a constant value for all the fittings. The fitted peaks for the thin films with thickness of 20, 100, and 200 nm are presented in Figure 14, Figure 15, and Figure 16, respectively.

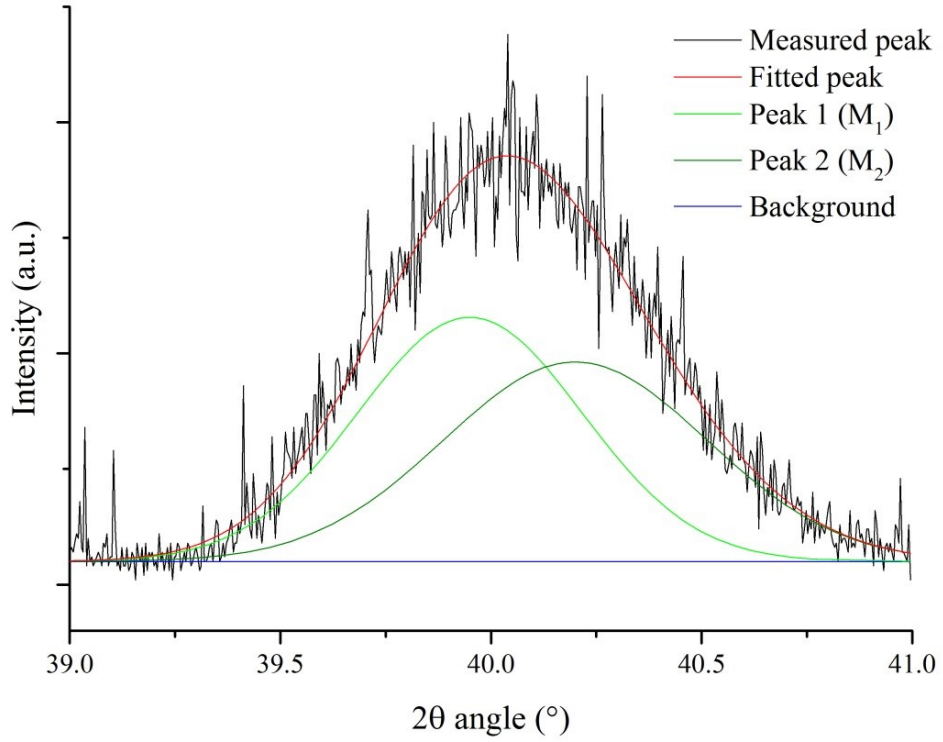

Figure 14. Measured and fitted XRD peak for the 20 nm thick film.

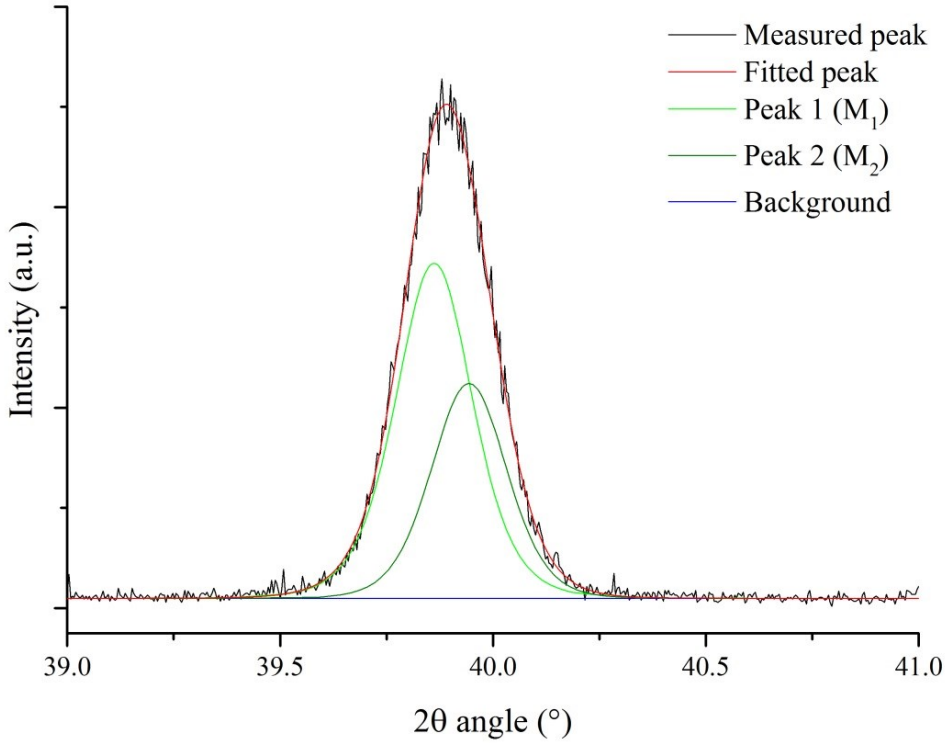

Figure 15. Measured and fitted XRD peak for the 100 nm thick film.

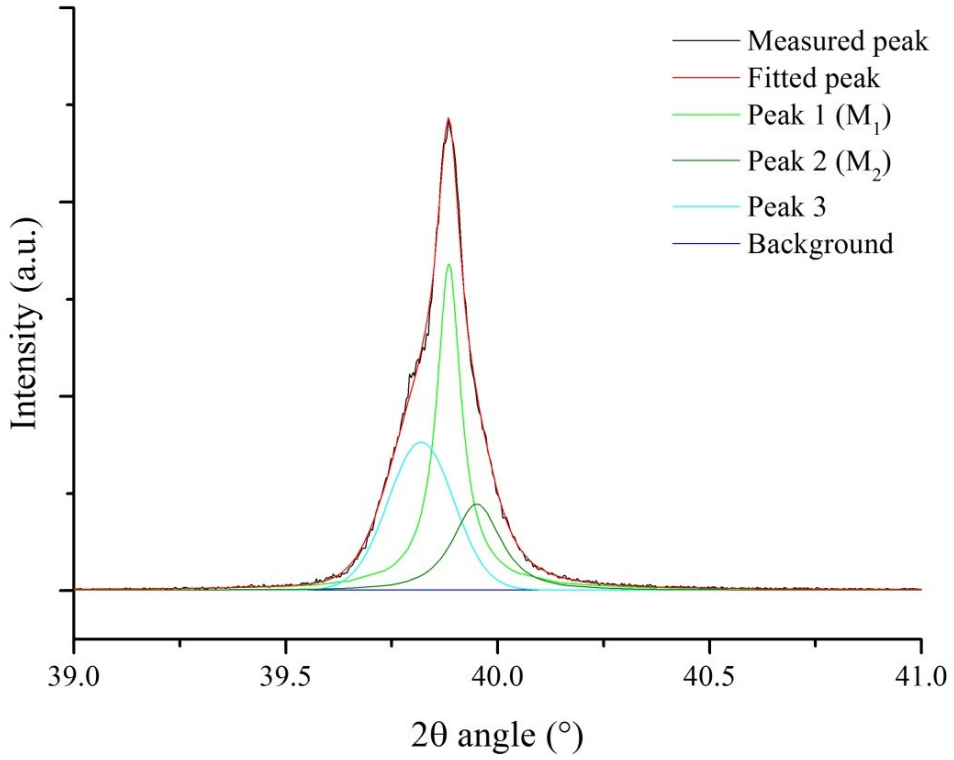

Figure 16. Measured and fitted XRD peak for the 200 nm thick film.

The five thinnest films were best fitted with two peaks, as shown in Figure 14 and Figure 15 for the 20 nm and 100 nm thick films. The measured peak from the films with thickness 30 and 100 nm could have been also been well-fitted with only one peak but the fitting with two peaks was in better agreement with the other fittings. The peak at a lower scattering angle is attributed to M_1 phase whereas the peak at a higher angle is attributed to M_2 phase. Interestingly, the two thickest films showed a sign of a third peak which is in a lower angle than the two other peaks, as in the case of the 200 nm thick film presented in Figure 16. The peaks from the three thickest films have a sharp top resulting from the narrow, high-intensity M_1 peak. It is noticed that the peak from the thinnest film is remarkably broad and the peak width is significantly reduced in the 30 nm film.

The interplanar spacings, *i.e.* d_{hkl} values, derived from the peak positions using Bragg's law given in equation (31) and the full width at half maximum (FWHM) values of the fitted peaks are plotted in Figure 17 and Figure 18 as a function of film thickness. Figure 17 shows the d_{010} and FWHM values for M_1 peaks while the d_{hkl} and FWHM values for M_2 and the third peak are presented in Figure 18.

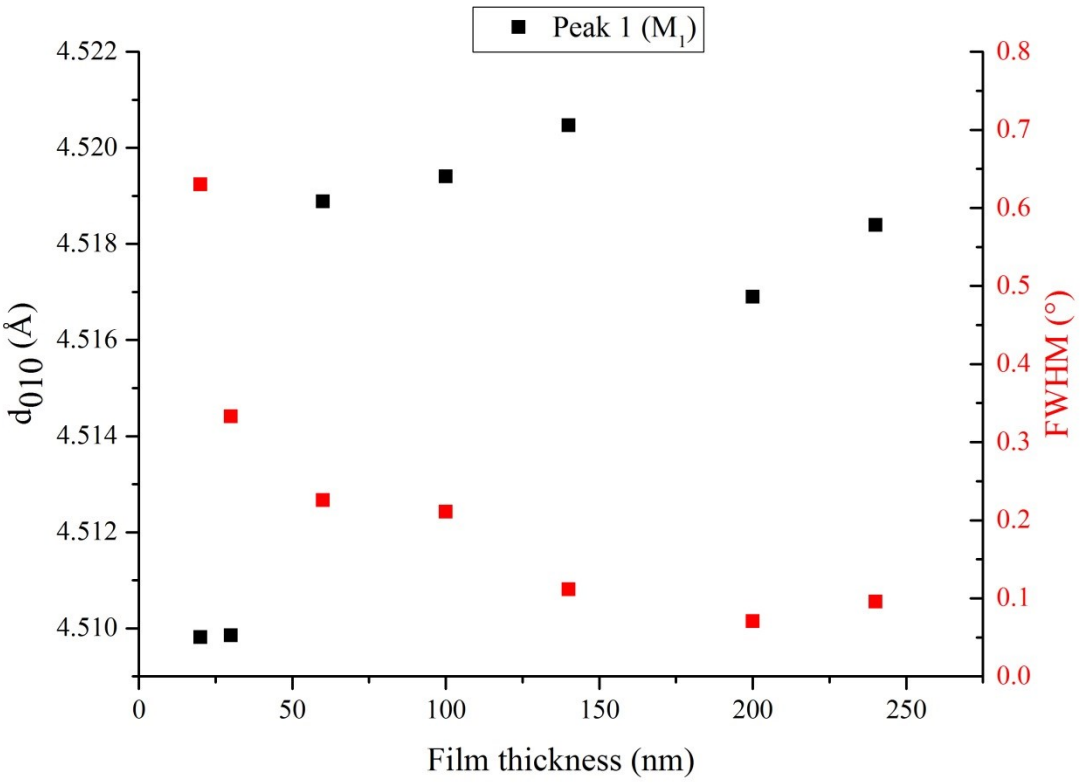

Figure 17. Calculated d_{010} and FWHM values for M_1 peak.

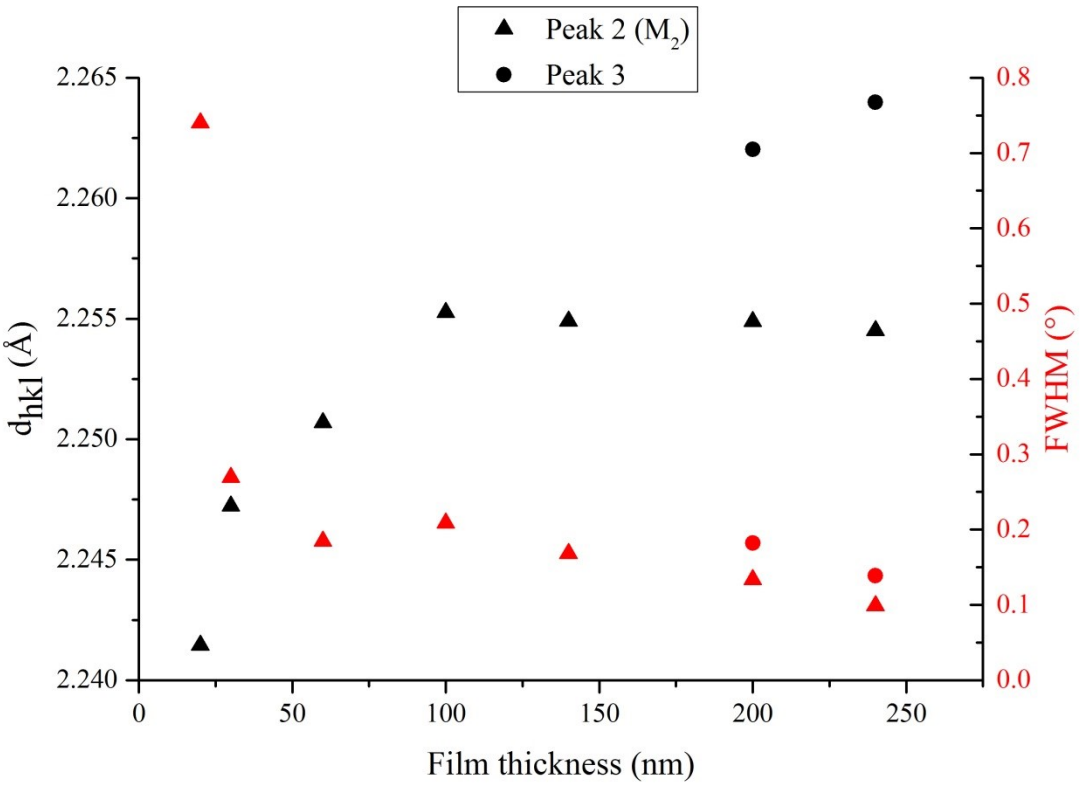

Figure 18. Calculated d_{hkl} and FWHM values for M_2 and the third peak.

The smallest spacing between the (010) planes of M_1 phase, which corresponds to the *b*-axis length, is observed in the two thinnest films. The *b*-axis length increases the most when the film thickness increases from 30 to 60 nm. Between thickness of 60 and 140 nm, the length increases with the film thickness until a sudden decrease occurs in the 200 nm thick film. In all of the films, the *b*-axis length of M_1 phase is clearly smaller than the bulk value 4.53 Å reported in Table 3. The peak position of M_2 phase is shifted to lower scattering angles with increasing film thickness when the film is from 20 to 100 nm thick, which can be seen from the increase of the respective d_{hkl} values. From the thickness of 100 nm onwards, the peak position is quite stabilized at 39.95° corresponding to an interplanar spacing of 2.255 Å. It is interesting to notice that this is also the highest angle where M_1 peak is found to be. In the two thinnest films, the (020) spacing of M_1 phase is also 2.255 Å. The calculated d_{hkl} value for the unknown third peak, which was observed in the two thickest films, increases with film thickness in a similar way as the d_{010} value of M_1 peak in the same films.

The FWHM value, which relates to the peak width, is largest in the thinnest film for both M_1 and M_2 peaks. The width of M_2 peak is greatly reduced in the second thinnest film, and the width monotonically decreases with increasing film thickness from the 100 nm film onwards. The width of M_1 peak is less abruptly reduced and the FWHM values are more dispersed. The width is still continuously reduced from the thinnest film to the 200 nm film. The 200 nm film exhibits the narrowest peak which is only 0.07° wide and corresponds to M_1 phase. The narrowest M_2 peak, which is 0.1° wide, is observed in the thickest film, and it is equivalent to the width of M_1 peak in the same film. The width of the third peak decreases with film thickness in a similar way as the width of M_2 peak in the same films.

7.3. GIXRD

Grazing incidence X-ray diffraction measurements were performed on two samples which were 60 and 240 nm thick. The measurement was done twice with the incident angle fixed at 3° and 5° while 2θ angle of 10° - 100° was scanned by the detector. The thicker film didn't show any peaks with either incident angles unlike the thinner film which produced a clear peak when incident angle was fixed at 3°. GIXRD measurement results for the 60 nm thick film are presented in Figure 19. As it can be seen, a small peak is also observed near the more intense peak when the measurement was done with the higher incident angle. According to equation (36), the diffraction occurs from planes which are tilted -31.3° from the surface plane in both cases. The *d*-spacing of these planes differs slightly because of the different peak positions. The peak at 68.7° corresponds to a d_{hkl} value of 1.37 Å, and the peak at 72.5° corresponds to a d_{hkl} value of 1.30 Å.

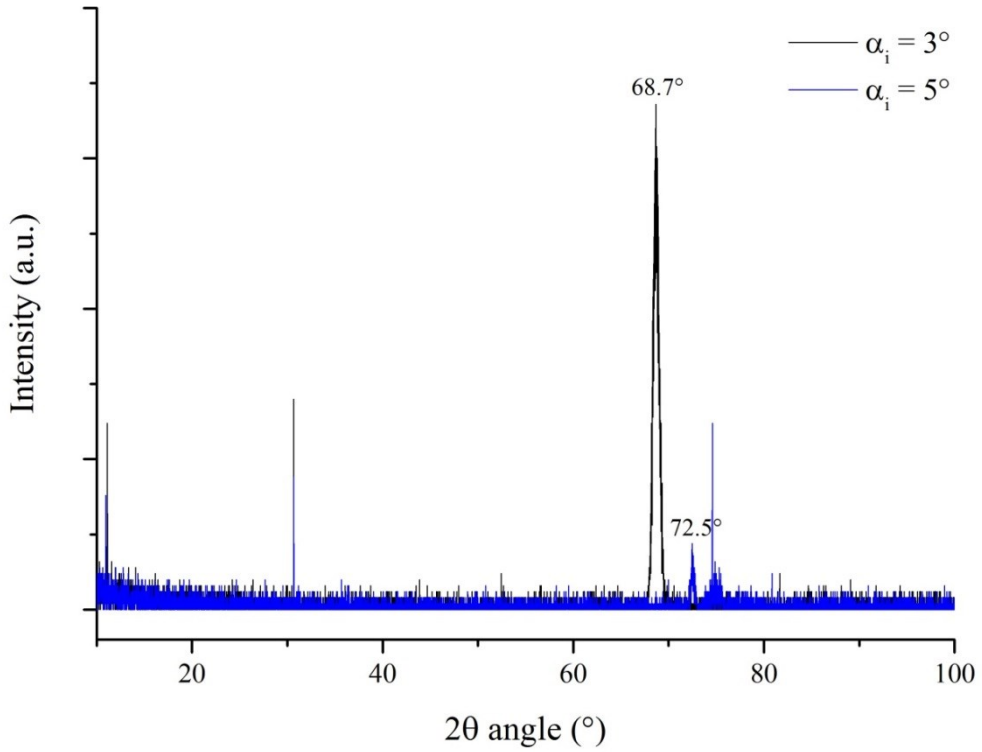

Figure 19. 2θ XRD pattern for the 60 nm thick film.

The reason why the thicker film didn't show any peaks is considered to be in the thickness dependency of the measurement configuration. The peaks observed in the thinner film are reflections from planes which are near the film-substrate interface, and because the thickness of the film is only 60 nm, the penetration depth of the X-rays is large enough to cause observable diffraction from those planes. For the 240 nm thick film, the X-rays don't penetrate deep enough to cause such diffraction from the film-substrate interface. Even when the measurement is performed with the higher incident angle, which should increase the penetration depth, the amount of X-rays reaching the interface is too small so the intensity of the peak seen in the thinner film at 72.5° is reduced even more and it is not observed.

7.4. Reciprocal Space Maps

Reciprocal space maps were recorded around the Al_2O_3 (0006) and M_1 (020) reflections using 2θ scan. Resolution was improved by using a 2-bounce monochromator. To reduce the overall measurement time, the detector was used in 1D mode. This makes it possible to record diffraction signals from an angle of 2.7° without moving the detector. The reciprocal space maps, displayed as Q_z versus Q_x plots, for the 20, 60, and 240 thick films are presented in Figure 20, Figure 21, and Figure 22, respectively. The shape of the maps result from the chosen scan type as indicated earlier in Figure 11. It is worth mentioning that this measurement configuration does not allow the determination of in-plane lattice parameters.

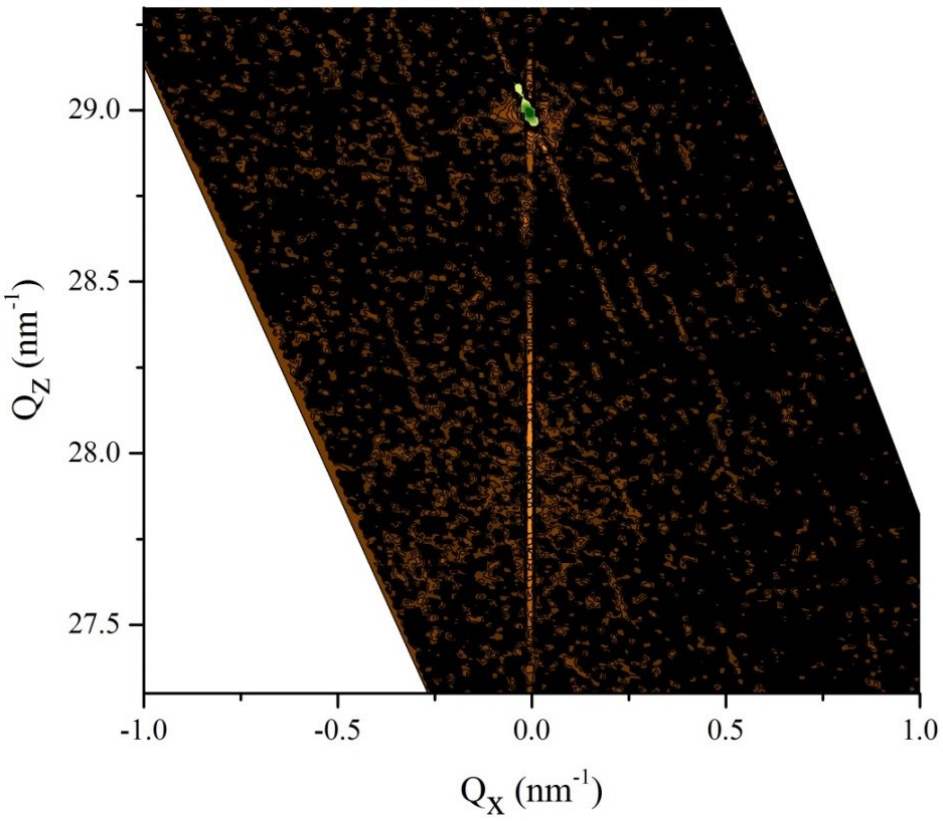

Figure 20. Reciprocal space map for the 20 nm film.

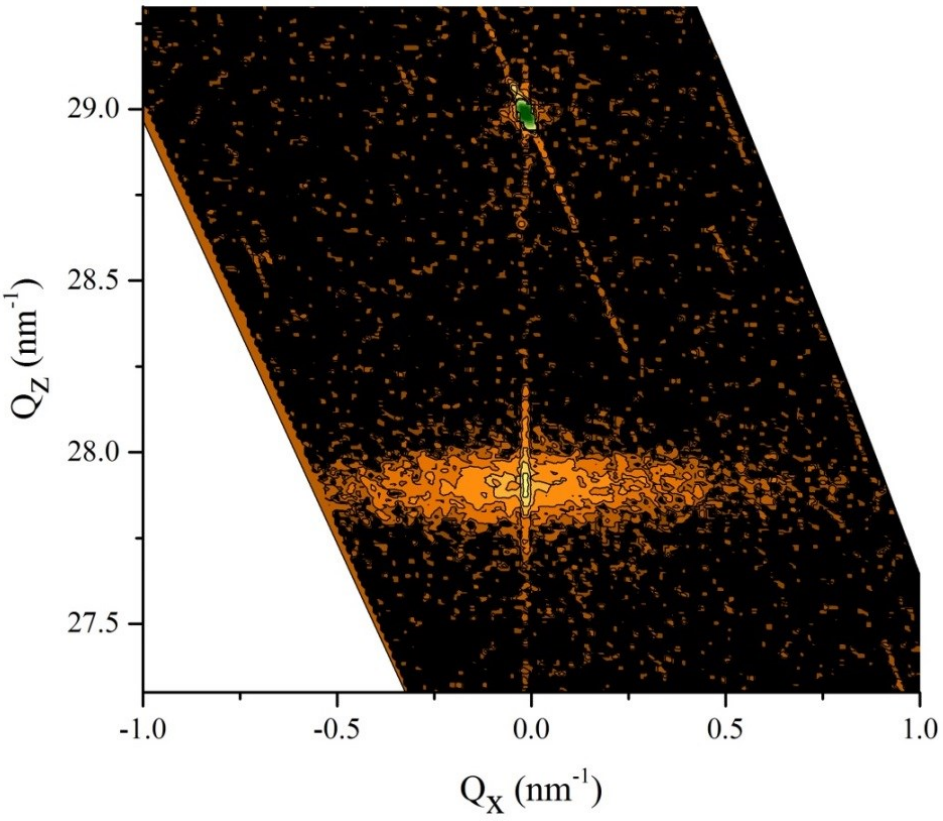

Figure 21. Reciprocal space map for the 60 nm film.

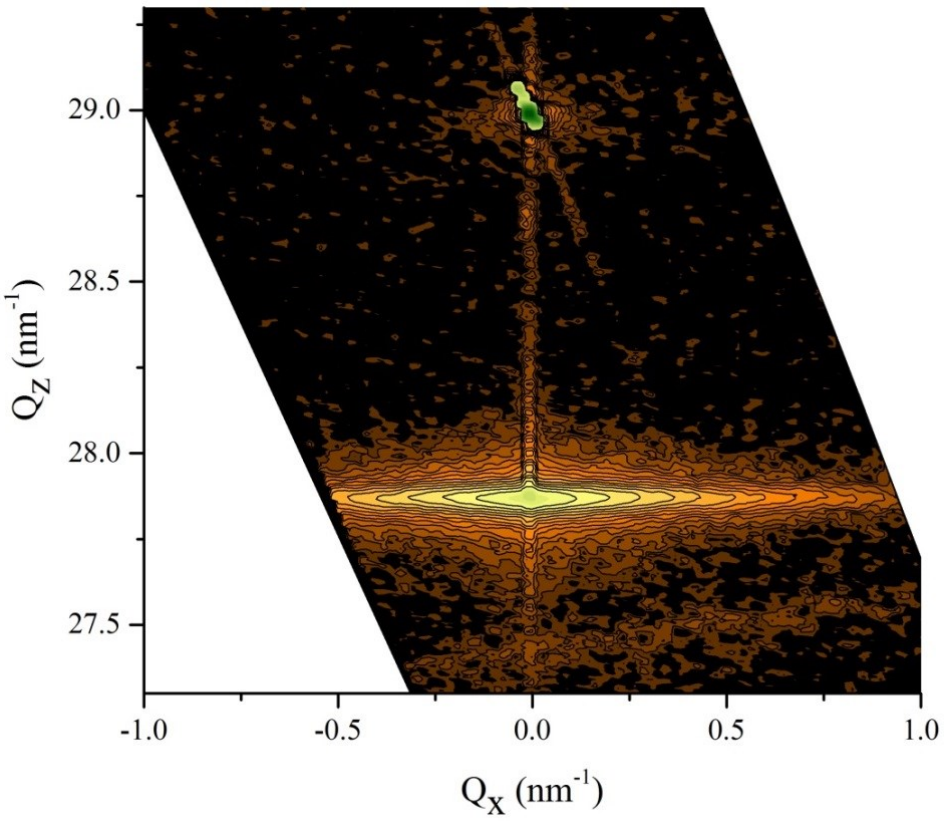

Figure 22. Reciprocal space map for the 240 nm film.

The high intensity diffraction spot which is colored with green is the (0006) reflection from the substrate. The streaks around this spot are typical for RSM measurements, and they arise from the finite resolution of the measurement configuration. The maps clearly confirm the epitaxial nature of the films since the region of highest intensity is directed along the vertical line where the substrate peak has its maximum, *i.e.* along $Q_x = 0$. Indeed, the film peak is exactly in the same Q_x position as the substrate peak in three films indicating high orientation of the film with respect to the substrate. The peak from the thickest film is misaligned the most compared to the substrate peak, but it only equals to inclination of 0.03° in real space.

The most noticeable change between the maps is the spread of intensities along the Q_x direction which is manifested by the tilting of the reflecting planes with respect to the substrate surface. A tilt of 1° in real space corresponds to a shift of about 0.5 nm^{-1} from the centermost position, *i.e.* $Q_x = 0$, in reciprocal space. This spread is seen to increase with film thickness indicating that the orientation of surface planes deteriorates in thicker films. Because the spread is directed horizontally, *i.e.* along the line where Q_z is constant, the spacing between the planes is, however, the same.

The variation of the interplanar spacings causes spread of intensities along the Q_z direction. It can be seen from the Figure 20 that the spacing between the reflecting planes is very distributed in the thinnest film indicating that the film is highly strained out-of-plane. The film is also highly oriented since no such spread is observed in the other direction. When the film thickness exceeds 20 nm, the intensity spread is reduced in the vertical direction, but at the same time, it is increased in the

horizontal direction. As a result, the intensity distribution becomes circular in the case of the 30 nm thick film. From the thickness of 60 nm onwards, the distribution becomes systematically more and more oval shaped, as seen in the reciprocal space maps for the 60 and 240 nm thick films shown in Figure 21 and Figure 22, respectively.

Intensity profiles along the vertical line where $Q_x = 0$ for the thinnest and the thickest film are shown in Figure 23. While the thickest film produces a clear peak corresponding to a certain average d_{hkl} value, the values are more distributed in the thinnest film resulting in a wide peak.

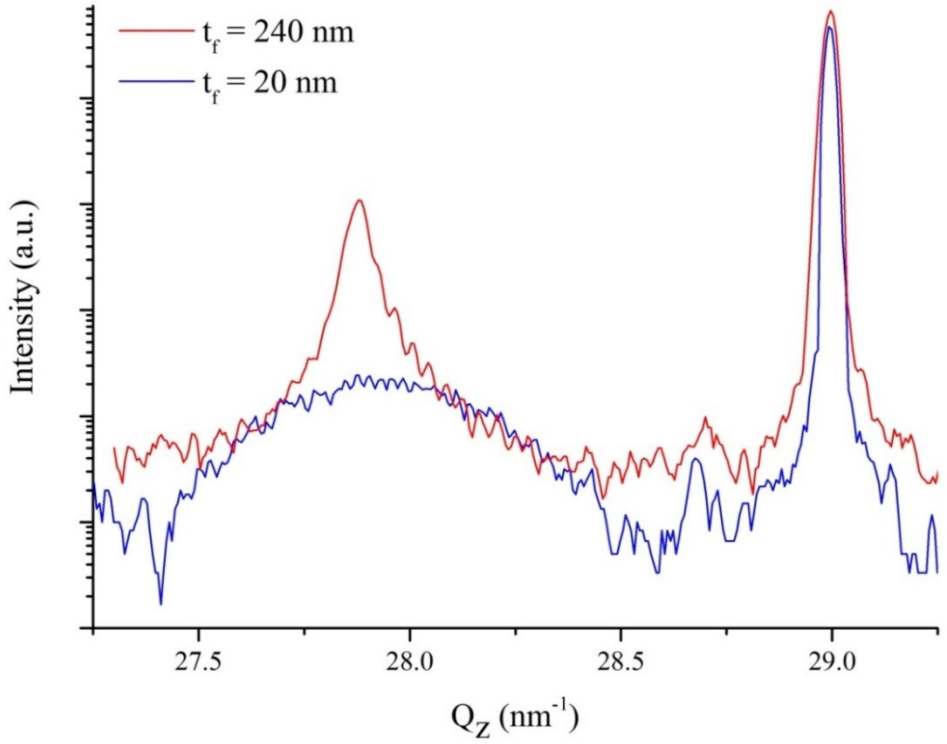

Figure 23. Intensity profiles along the vertical line $Q_x = 0$ where substrate peak has its maximum for the thinnest and thickest films.

7.5. Raman Spectroscopy

Despite the intensity variations, Raman measurements didn't reveal any thickness-dependent changes. Raman intensities for the thinnest and thickest film collected from a range of 50 to 1200 cm^{-1} are presented in Figure 24. The spectra consist of peaks at 130, 200, 225, 270, 310, 340, 390, 440, 500, 620, and 825 cm^{-1}. There also seems to be a peak at 580 cm^{-1} on the left side of the strongest and widest peak. The peaks at 420 and 750 cm^{-1} present in the spectrum for the thinnest film are from the Al_2O_3 substrate. These peaks were not observed from the thickness of 100 nm onwards. Though it is hard distinguish M_1 and M_2 phases, Raman results clearly verify that all the films are pure VO_2 films.

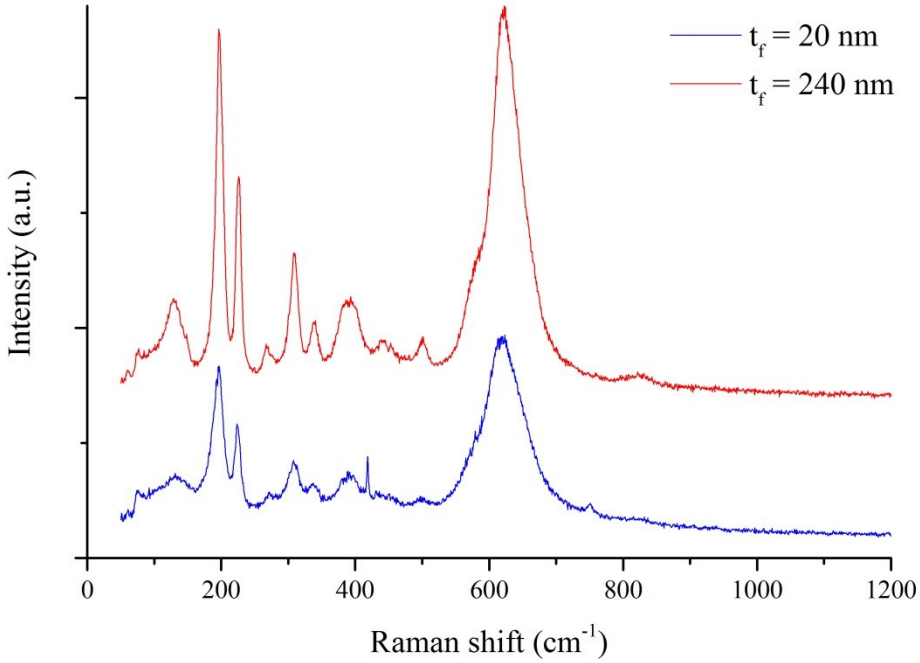

Figure 24. Raman spectra for the thinnest and thickest film.

An intensity sweep was also performed for the thinnest and thickest films. In this experiment, Raman spectrum was collected multiple times with increasing laser intensities. The thickest film was observed to go to the metallic phase as proven by Raman spectrum shown in Figure 25. The spectrum of the metallic phase has an intense background with some broad peaks, such as the ones at 250, 390, and 520 cm^{-1}. The thinnest film, however, remained in the insulating phase. The reason for this is unclear, but because of the reduced film thickness, the heat conduction of the substrate, for example, may have a significant effect.

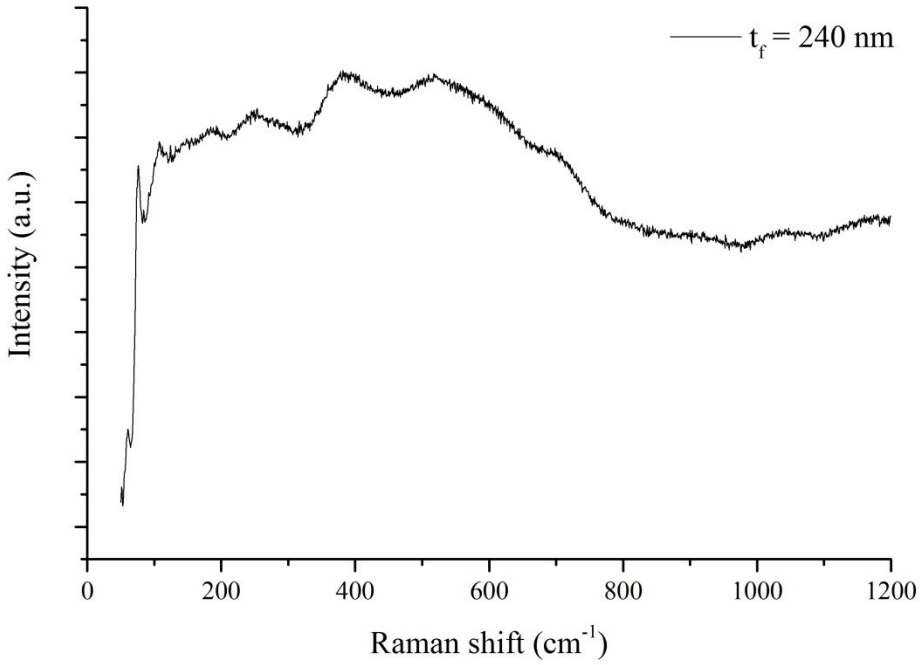

Figure 25. Raman spectrum for the metallic phase of VO_2.

7.6. Surface Morphology

The surface morphology of the thin films was examined by atomic force microscope performed in tapping mode. AFM images for the 30, 60, and 240 nm thick films are presented in Figure 26, Figure 28, and Figure 30, respectively. Three-dimensional images of the surface for the 30 and 60 nm thick films are also presented in Figure 27 and Figure 29, respectively.

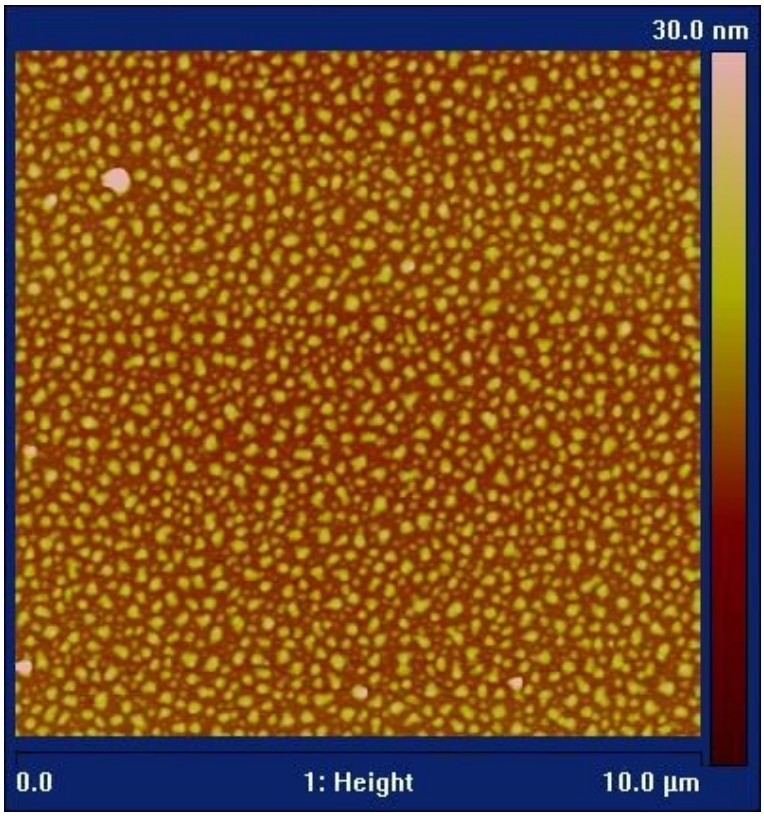

Figure 26. Surface morphology of the 30 nm thick film.

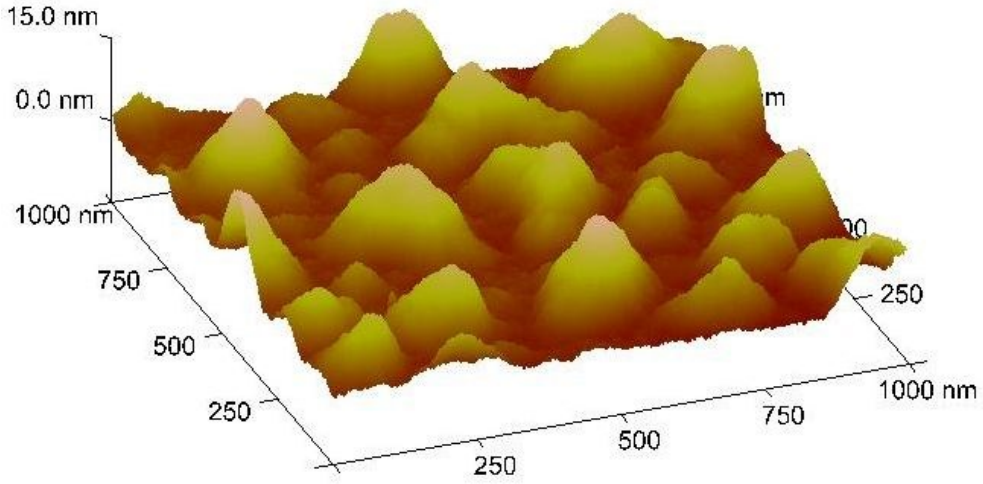

Figure 27. Three-dimensional AFM image for the 30 nm thick film.

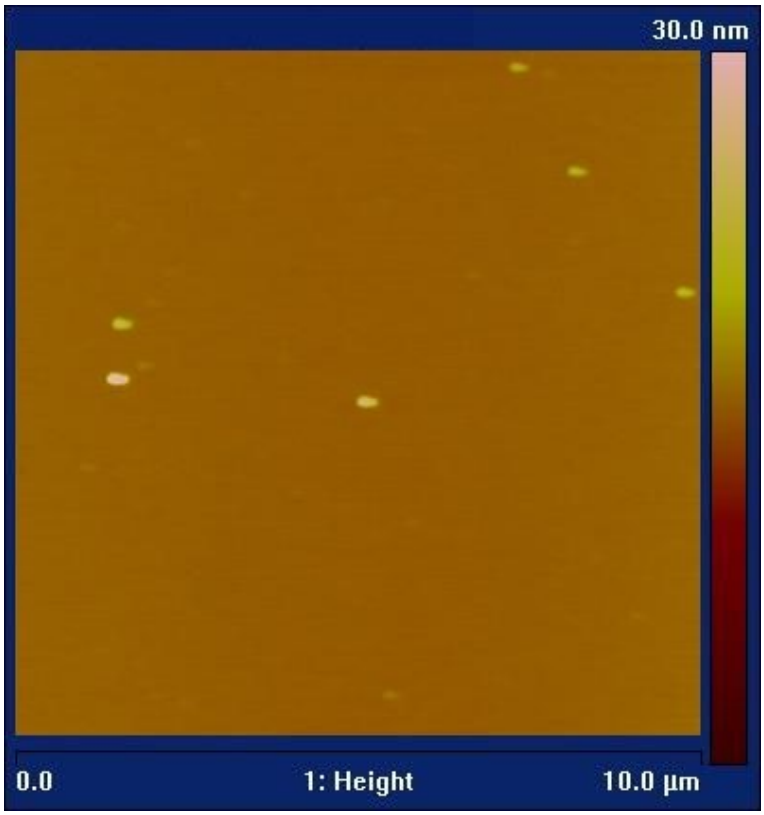

Figure 28. Surface morphology of the 60 nm thick film.

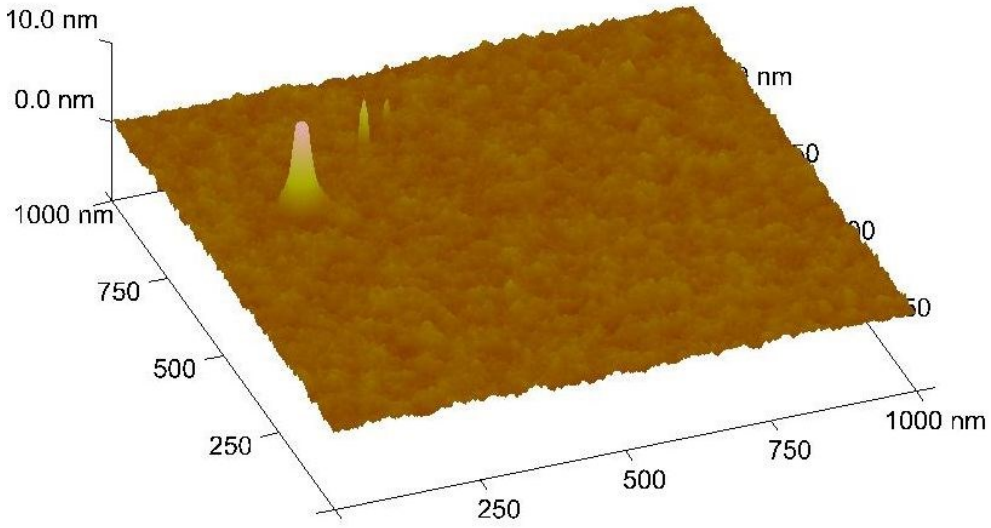

Figure 29. Three-dimensional AFM image for the 60 nm thick film.

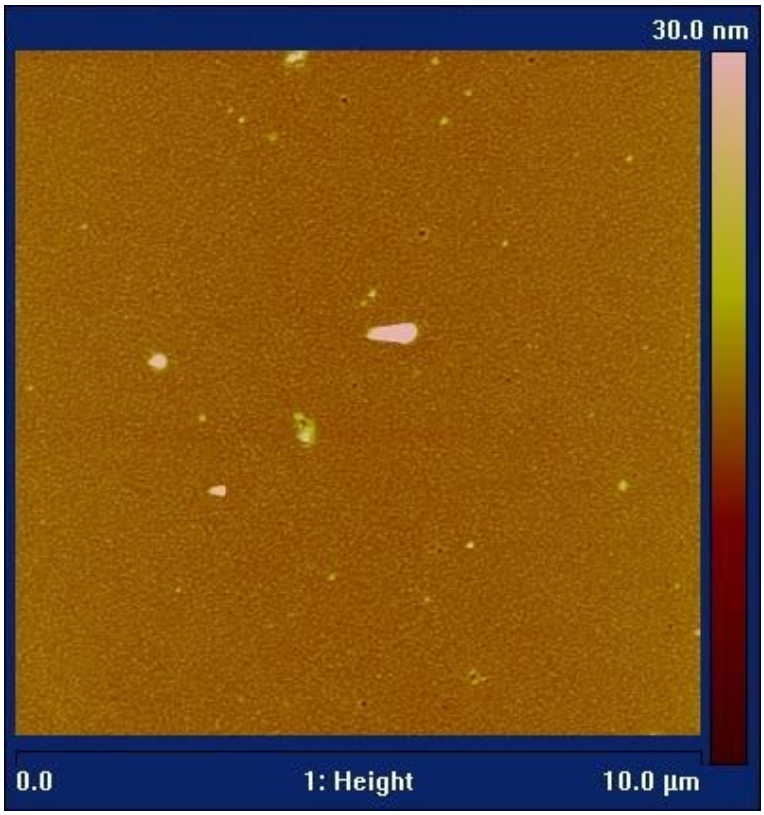

Figure 30. Surface morphology of the 240 nm thick film.

The 30 nm thick film has by far the roughest surface with the root mean square (RMS) roughness R_q of 2.9 nm. The second roughest surface is observed in the thinnest and thickest films with the average roughness of about 0.75 nm, which is almost four times less than in the 30 nm thick film. The most flat and smooth surface is observed in the 60 nm thick film whose AFM image is shown Figure 28. The RMS roughness R_q of the film is only 0.12 nm. The contrast between the roughest and the smoothest film is obvious when comparing the 3D images presented in Figure 27 and Figure 29. There are some larger particulates present in the surface of the films, which is a characteristic feature of the pulsed laser deposition method. To diminish their effect, the R_q values were estimated from a smaller area than the 100 µm^2 imaging area where no distinct particulates were present. R_q values are plotted in Figure 31 as a function of film thickness. It can be seen that from the thickness of 60 nm onwards, the average roughness scales quite well with the film thickness.

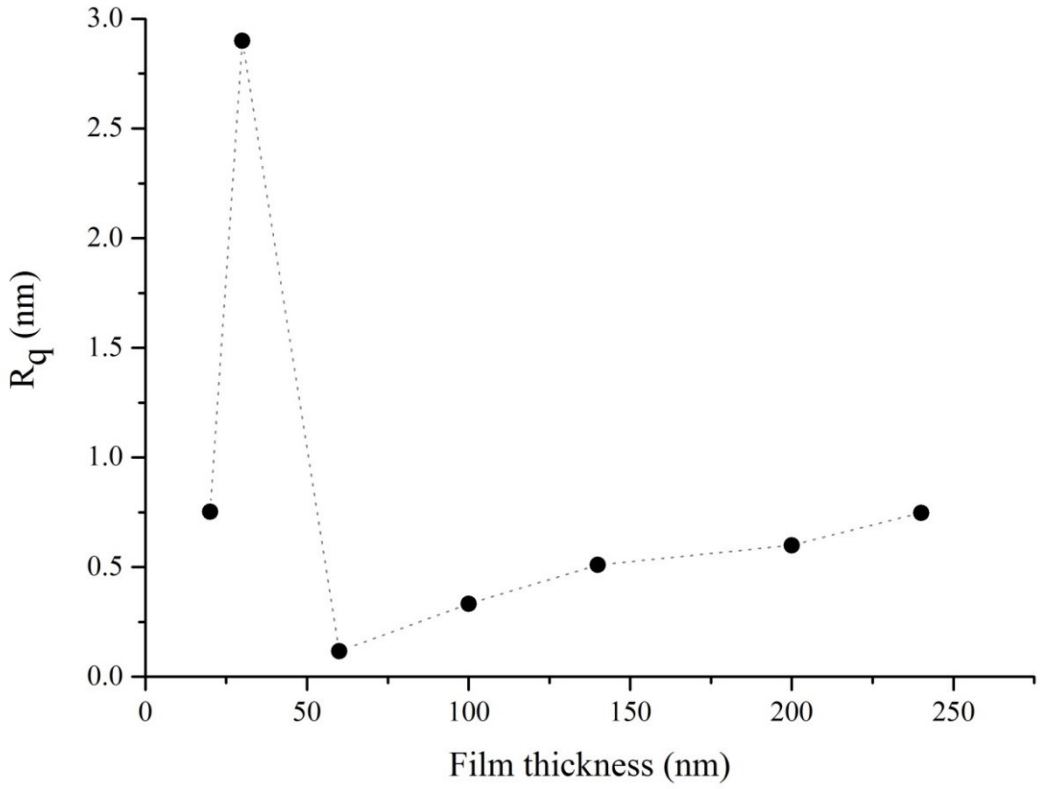

Figure 31. Measured root mean square roughness R_q values.

7.7. MIT Characteristics

The temperature-dependent resistivity of the films is shown in Figure 32 and Figure 33. All the films exhibits the transition from the low-temperature insulating phase to the high-temperature metallic phase, but the transition behavior is quite different depending on the film thickness. In thinner films, the transition seems to begin earlier since the resistivity change is stronger at lower temperatures than in the thicker films. The resistivity change is, however, not so sharp near the transition point which leads to much wider transition. In thicker films, the transition is more pronounced since it is delayed to higher temperatures, and it occurs at much narrower temperature range.

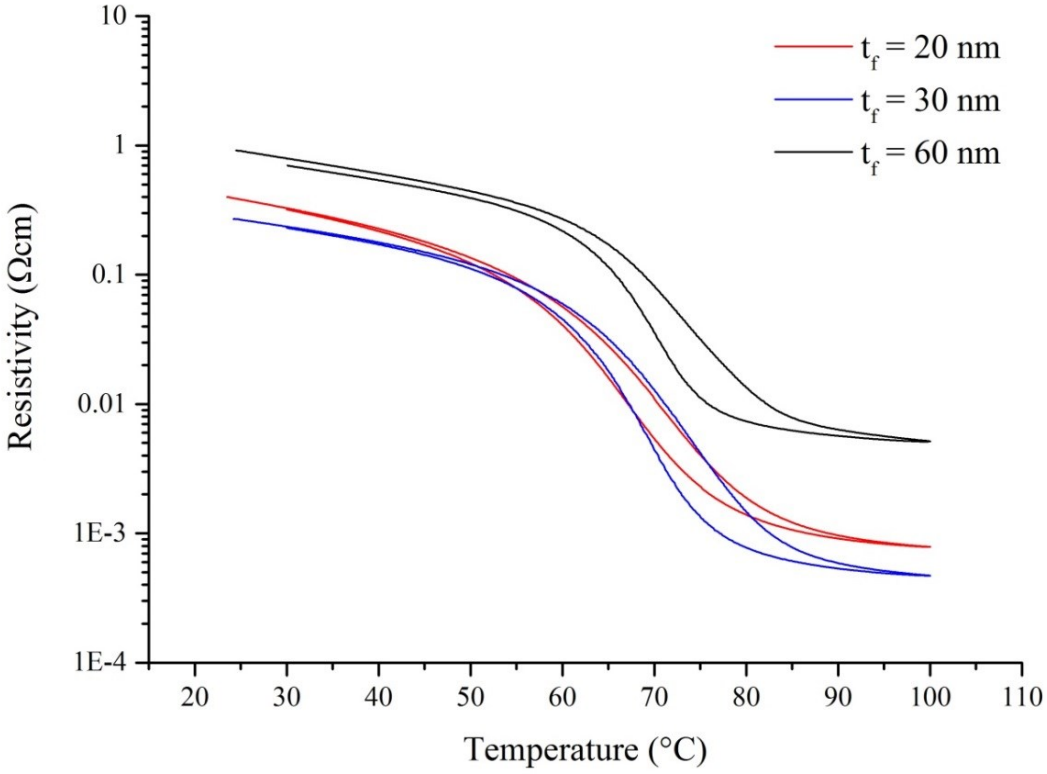

Figure 32. Transition curves for the three thinnest films.

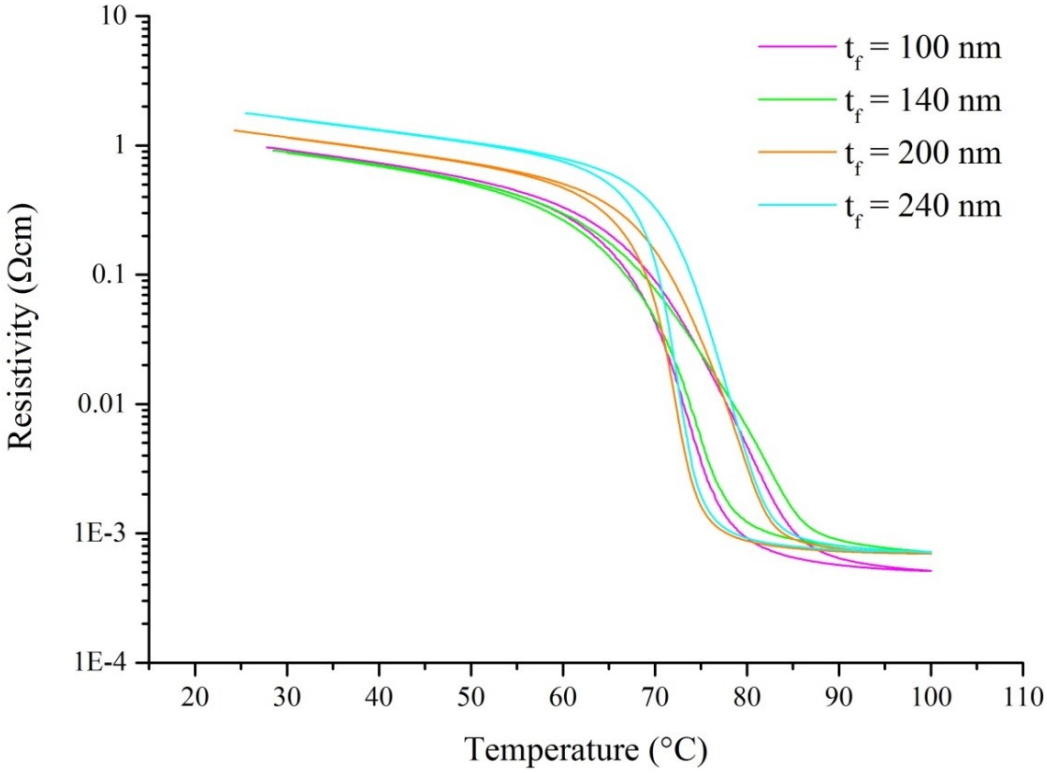

Figure 33. Transition curves for the four thickest films.

The room-temperature resistivity of the films scales quite well with the film thickness so the contrast between the resistivity of the insulating phase and the metallic phase is higher in thicker films. The resistivity of the films at 30 °C ranges from 0.24 to 1.6 Ωcm. The highest resistivity is measured in thickest film and the lowest resistivity in the 30 nm thick film. Before the transition, the films show behavior similar to semiconductors since the resistivity decreases with increasing temperature. The highest contrast between the high- and low-temperature resistivity, which is over three orders in magnitude, is measured in the thickest film. The lowest contrast, which is only two orders in magnitude, is observed in the 60 nm thick film. This film has by far the highest resistivity in the metallic phase making its transition curve most distinguishable against the rest of the curves. The high-temperature resistivity of the 60 nm thick film is 5.2×10^{-3} Ωcm while it ranges from 4.7×10^{-4} to 7.9×10^{-4} Ωcm for the rest of the films. Above the transition, the resistivity is seen to still decrease with increasing temperature which suggests that the films are not fully in a metallic state.

The hysteresis behavior of the resistivity curves is seen to become more asymmetric as the thickness of the film increases. The derivative of the log ρ curve is presented in Figure 34 and Figure 35 for the thinnest and thickest film, respectively, illustrating the differences in the transition behavior. In the thinnest film, the transition is very symmetric as seen in the derivative curves which are very similar in shape. The magnitude of the resistivity change is also very comparable during the heating and cooling cycle. When the film thickness increases, the resistivity change becomes more abrupt but the contrast between the resistivity change measured upon heating and cooling becomes more distinct leading to more asymmetric hysteresis loop. As seen in Figure 35, the transition occurs over a wider temperature range during the heating cycle while much sharper transition is observed during the cooling cycle.

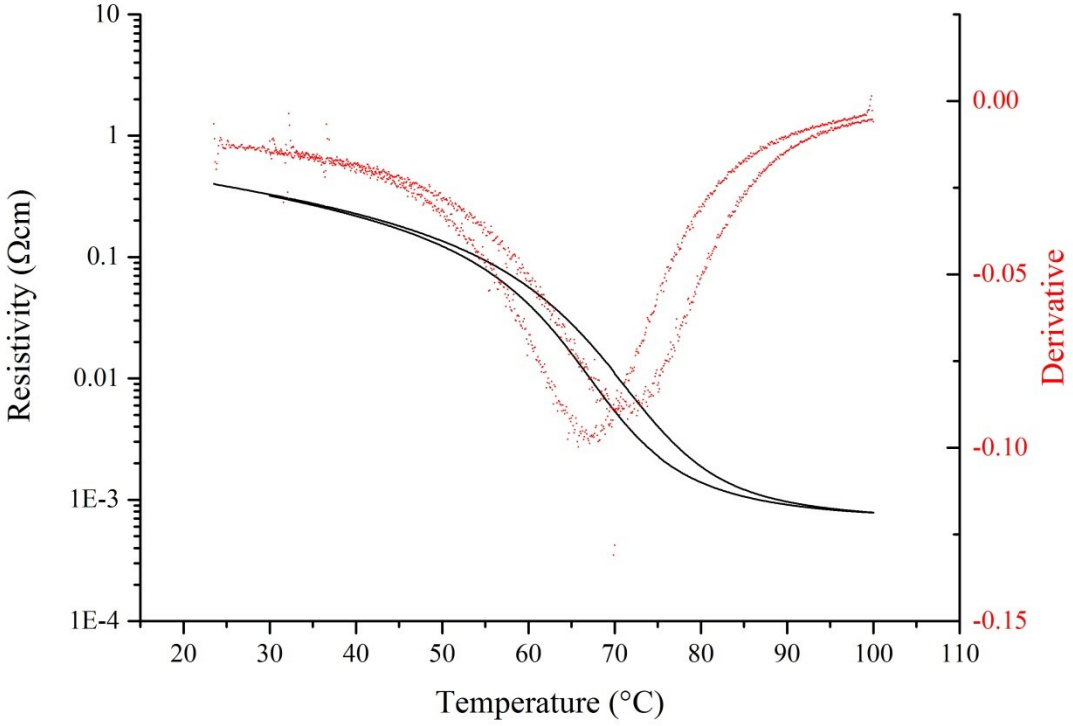

Figure 34. Transition behavior of the 30 nm thick film.

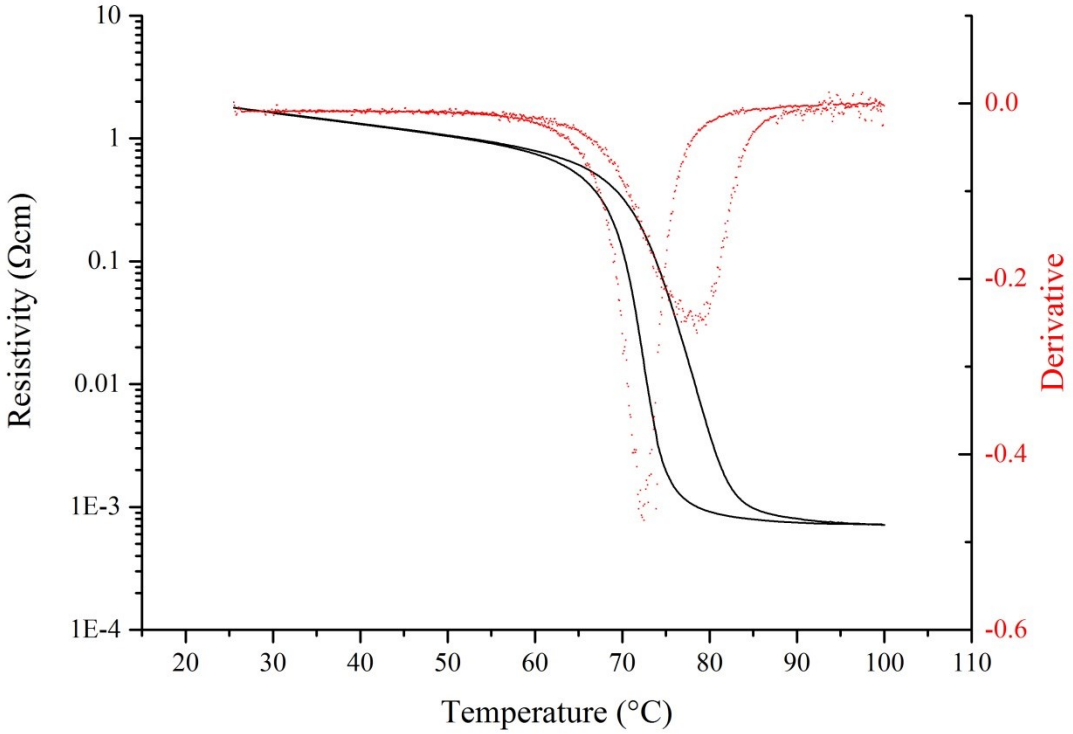

Figure 35. Transition behavior of the 240 nm thick film.

The transition temperatures T_{MIT} and T_{cool}, which were derived from the peak positions in the log ρ derivative curve measured upon heating and cooling, respectively, are plotted in Figure 36. The difference between the transition temperatures, which is a measure for the hysteresis, is also displayed in the same figure. In all of the films, the metal-insulator transition occurs above 70 °C, which is at higher temperature than the bulk value, and the difference between the highest and lowest T_{MIT} is over 10 °C. The difference between the highest and lowest transition temperatures measured upon cooling is 7.3 °C. The lowest transition temperatures are observed to be in the three thinnest films, which have T_{MIT} values between 71.7 and 74.3 °C. In the four thickest films, the transition occurs between 78.8 and 82.3 °C. The thinnest film has the lowest T_{MIT} and T_{cool} values. The 220 nm thick film has the highest transition temperatures and also the widest hysteresis, which is almost 8 °C. The smallest hysteresis, which is 3 °C, is observed in the 60 nm thick film.

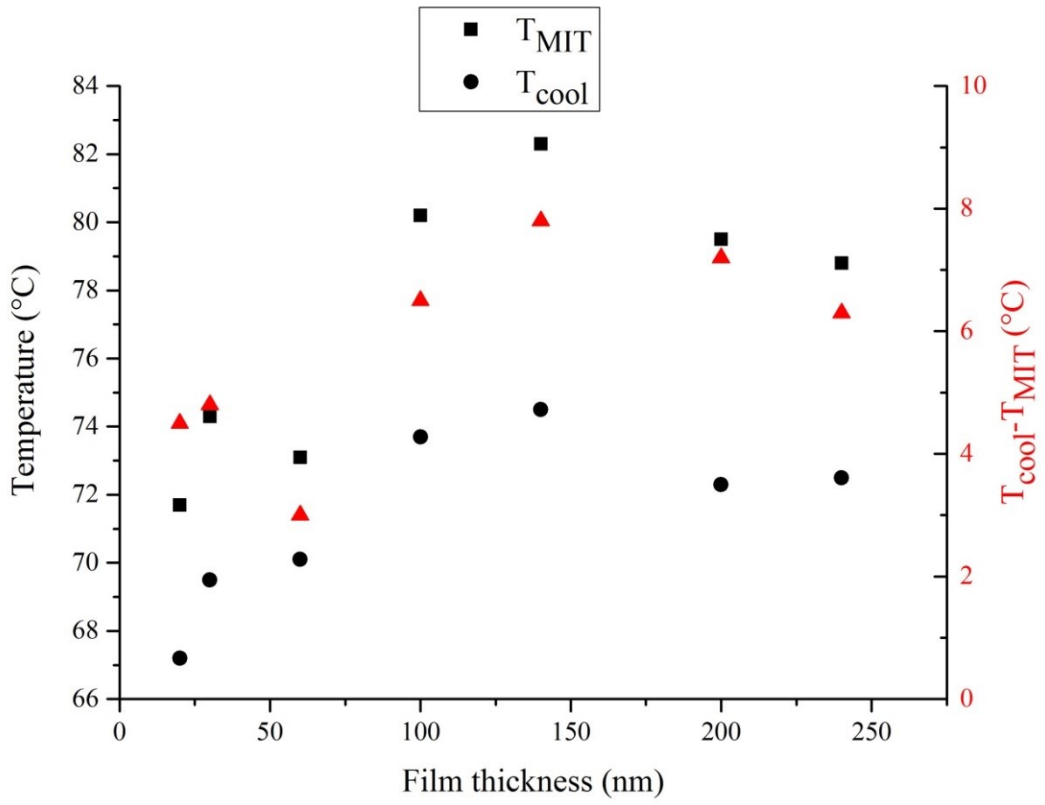

Figure 36. Transition temperatures T_{MIT} and T_{cool} for the heating and cooling cycles, respectively. The difference between the transition temperatures is also displayed.

8. DISCUSSION

X-ray diffraction measurements revealed that the films had peaks from both M_1 and M_2 phases at room temperature. A third peak, whose origin remained unsolved, was also observed in the two thickest films. Based on the behavior of this third peak in temperature-dependent XRD measurements, the peak has been attributed to the metallic phase elsewhere [54]. The out-of-plane *d*-spacing of M_2 phase was smaller in the three thinnest films, which were 20 – 60 nm thick, than in thicker films indicating that M_2 phase was compressively strained out-of-plane in thinner films. Because the *d*-spacing varied only by a small amount in thicker films, which were 100 – 240 nm thick, it can be assumed that the strain in M_2 phase becomes relaxed when the film thickness exceeds 60 nm. The *b*-axis of M_1 phase, which was directed out-of-plane, was noticed to be compressed in all of the films. The *b*-axis was most compressed in two thinnest films. Since M_2 phase was stabilized and all the films exhibited the metal-insulator transition above 70 °C, it can be assumed that the *a*-axis of M_1 phase and the *b*-axis of M_2 phase, which relate to the *c*-axis of the metallic phase, are tensile strained in all of the films.

The measured metal-insulator transition curves showed that the transition temperatures were different between the thinner and thicker films. The transition occurred between 71 – 75 °C in the three thinnest films and between 78 - 83 °C in the four thickest films. It is thought that the transition is controlled by M_2 phase in the three thinnest films while it is controlled by M_1 phase in the four thickest films. M_2 phase is stabilized right in the film-substrate interface where the impact of strain is strongest and therefore controls the transition in thinner films. It seems that when the film is 60 – 100 nm thick, the strain begins to be insufficient to stabilize M_2 phase. When the film thickness increases, the proportion of M_1 phase compared to M_2 phase increases, and M_1 phase begins to control the transition. The change in the volume fraction of the phases may be responsible for the observed increase of the room-temperature resistivity when the film thickness increases. This would indicate that M_2 phase has lower resistivity than M_1 phase.

The rate of the resistivity change was also seen to differ in thinner and thicker films. The high strain in thinner films seems to result in transition which is clearly prolonged. When the thickness increases, the transition becomes more abrupt. The thicker films produced much narrower XRD peaks, which is an indicative of reduced microstrain. Therefore, it can be concluded that reduction of strain results in more pronounced MIT characteristics. Though the transition occurs in narrower temperature range, the hysteresis becomes more asymmetric in thicker films. The symmetric hysteresis is typical for thin films, and it is caused by the substrate-induced mechanical stress. In thicker films, relaxation leads to strain gradient in the direction of the film thickness and induces asymmetry in the hysteresis.

The reciprocal space maps revealed that the planes which are parallel to the surface plane become more tilted in thicker films. This may result from strain relaxation which causes misorientation of the crystallites at the same time when the strain in the film is reduced in thicker films. The increasing misorientation might be responsible for the increased surface roughness in the films which were thicker than 60 nm. The surface roughness changed the most between the three thinnest films which might be caused by the variation of M_1 and M_2 phases. The surface is much rougher in the two thinnest films because M_2 phase is present at the surface, but in the 60 nm film, M_1 phase has evened out the surface. The surface roughness was

0.75 Å and 2.9 Å in the 20 nm and 30 nm thick films, respectively, while in the 60 nm film, it was only 0.12 Å.

9. CONCLUSION

When the film is cooled down from the deposition temperature, the vanadium dioxide film, which was initially grown in the metallic phase, transforms to its low-temperature phases and becomes subjected to strain due to the lattice mismatch between the film and the substrate. Strain was observed to stabilize M_2 phase together with M_1 phase and induce changes in their out-of-plane lattice parameters. X-ray diffraction is a powerful method to monitor these changes although some challenges are encountered when dealing with thin films. It has to be kept in mind that the lattice parameters were derived from fitted peaks and the fitting procedure can be quite ambiguous. Nevertheless, the measurements managed to give some insight about the strain and its evolution when the thickness of the vanadium dioxide thin film changes. Clear thickness-dependent changes were observed in the recorded reciprocal space maps where the orientation of the film was noticed to deteriorate with increasing film thickness as a result of strain relaxation. This effect caused the surface roughness to increase in thicker films.

Based on the observations, the metal-insulator transition behavior of the films could be classified into two classes: M_1 and M_2 controlled MIT. M_2 phase controls the transition in thinner films where the impact of strain is stronger. This results in a broader transition which occurs at lower temperatures. In thicker films, the transition is controlled by M_1 phase, and it occurs at higher temperatures. The reduction of strain leads to more abrupt transition, and because of the higher resistivity of M_1 phase, the magnitude of the resistivity change is stronger in thicker films.

10. REFERENCES

[1] Beiser A. (2003) Concepts of Modern Physics, 6th Edition. McGraw-Hill, New York, 530 p.

[2] Kasap S.O. (2006) Principles of Electronic Materials and Devices, 3rd Edition. McGraw-Hill, Boston, 874 p.

[3] Kittel C. (2005) Introduction to Solid State Physics, 8th Edition. Wiley, Hoboken, N.J., 704 p.

[4] Ibach H. & Lüth H. (2009) Solid-State Physics: An Introduction to Principles of Materials Science, 4th Edition. Springer, Berlin, 533 p.

[5] Birkholz M. (2006) Thin Film Analysis by X-Ray Scattering. Wiley, Weinheim, 378 p.

[6] Pietsch U., Holy V. & Baumbach T. (2004) High-Resolution X-Ray Scattering: From Thin Films to Lateral Nanostructures, 2nd Edition. Springer, New York, 408 p.

[7] Yang Z., Ko C. & Ramanathan S. (2011) Oxide electronics utilizing ultrafast metal-insulator transitions. Annual Review of Materials Research, vol. 41, pp. 337-367.

[8] Ruzmetov D. & Ramanathan S. (2010) Metal-Insulator Transition in Thin Film Vanadium Dioxide. In: Ramanathan S. (ed.) Thin Film Metal-Oxides: Fundamentals and Applications in Electronics and Energy. Springer, New York, pp. 51-94.

[9] Imada M., Fujimori A. & Tokura Y. (1998) Metal-insulator transitions. Reviews of Modern Physics, vol. 70, no. 4, pp. 1039-1263.

[10] Grüner G. (1988) The dynamics of charge-density waves. Reviews of Modern Physics, vol. 60, no. 4, pp. 1129-1181.

[11] Belitz D. & Kirkpatrick T.R. (1994) The Anderson-Mott transition. Reviews of Modern Physics, vol. 66, no. 2, pp. 261-380.

[12] Evers F. & Mirlin A.D. (2008) Anderson transitions. Reviews of Modern Physics, vol. 80, no. 4, pp. 1355-1417.

[13] Zaanen J., Sawatzky G.A. & Allen J.W. (1985) Band gaps and electronic structure of transition-metal compounds. Physical Review Letters, vol. 55, no. 4, pp. 418-421.

[14] Zylbersztejn A. & Mott N.F. (1975) Metal-insulator transition in vanadium dioxide. Physical Review B, vol. 11, no. 11, pp. 4383-4395.

[15] Demeter M., Neumann M. & Reichelt W. (2000) Mixed-valence vanadium oxides studied by XPS. Surface Science, vol. 454, no. 1, pp. 41-44.

[16] Eyert V. (2002) The metal-insulator transitions of VO_2: A band theoretical approach. Annalen der Physik (Leipzig), vol. 11, no. 9, pp. 650-702.

[17] Marezio M., McWhan D.B., Remeika J.P. & Dernier P.D. (1972) Structural aspects of the metal-insulator transitions in Cr-doped VO_2. Physical Review B, vol. 5, no. 7, pp. 2541-2551.

[18] Pouget J.P., Launois H., D'Haenens J.P., Merenda P. & Rice T.M. (1975) Electron localization induced by uniaxial stress in pure VO_2. Physical Review Letters, vol. 35, no. 13, pp. 873-875.

[19] Rice T.M., Launois H. & Pouget J.P. (1994) Comment on "VO_2: Peierls or Mott-Hubbard? A view from band theory". Physical Review Letters, vol. 73, no. 22, pp. 3042.

[20] Pouget J.P. *et al.* (1974) Dimerization of a linear Heisenberg chain in the insulating phases of $V_{1-x}Cr_xO_2$. Physical Review B, vol. 10, no. 5, pp. 1801-1815.

[21] Grinolds M.S., Lobastov V.A., Weissenrieder J. & Zewail A.H. (2006) Four-dimensional ultrafast electron microscopy of phase transitions. Proceedings of the National Academy of Sciences of the United States of America, vol. 103, no. 49, pp. 18427-18431.

[22] McWhan D.B., Marezio M., Remeika J.P. & Dernier P.D. (1974) X-ray diffraction study of metallic VO_2. Physical Review B, vol. 10, no. 2, pp. 490-495.

[23] Wentzcovitch R.M., Schulz W.W. & Allen P.B. (1994) VO_2: Peierls or Mott-Hubbard? A view from band theory. Physical Review Letters, vol. 72, no. 21, pp. 3389-3392.

[24] Cavalleri A., Dekorsy T., Chong H.H.W., Kieffer J.C. & Schoenlein R.W. (2004) Evidence for a structurally-driven insulator-to-metal transition in VO_2: A view from the ultrafast timescale. Physical Review B - Condensed Matter and Materials Physics, vol. 70, no. 16, pp. 1-4.

[25] Kim H.T. *et al.* (2006) Monoclinic and correlated metal phase in VO_2 as evidence of the Mott transition: Coherent phonon analysis. Physical Review Letters, vol. 97, no. 26, pp. 1-4.

[26] Laad M.S., Craco L. & Müller-Hartmann E. (2006) Metal-insulator transition in rutile-based VO_2. Physical Review B - Condensed Matter and Materials Physics, vol. 73, no. 19, pp. 1-7.

[27] Biermann S., Poteryaev A., Lichtenstein A.I. & Georges A. (2005) Dynamical singlets and correlation-assisted Peierls transition in VO_2. Physical Review Letters, vol. 94, no. 2, pp. 1-4.

[28] Koethe T.C. *et al.* (2006) Transfer of spectral weight and symmetry across the metal-insulator transition in VO_2. Physical Review Letters, vol. 97, no. 11, pp. 1-4.

[29] Haverkort M.W. *et al.* (2005) Orbital-assisted metal-insulator transition in VO_2. Physical Review Letters, vol. 95, no. 19, pp. 1-4.

[30] Shin S. *et al.* (1990) Vacuum-ultraviolet reflectance and photoemission study of the metal-insulator phase transitions in VO_2, V_6O_{13}, and V_2O_3. Physical Review B, vol. 41, no. 8, pp. 4993-5009.

[31] Rosevear W.H. & Paul W. (1973) Hall effect in VO_2 near the semiconductor-to-metal transition. Physical Review B, vol. 7, no. 5, pp. 2109-2111.

[32] Aetukuri N.B. *et al.* (2013) Control of the metal-insulator transition in vanadium dioxide by modifying orbital occupancy. Nature Physics, vol. 9, no. 10, pp. 661-666.

[33] Paquet D. & Leroux-Hugon P. (1980) Electron correlations and electron-lattice interactions in the metal-insulator, ferroelastic transition in VO_2: A thermodynamical study. Physical Review B, vol. 22, no. 11, pp. 5284-5301.

[34] Ruzmetov D., Senanayake S.D., Narayanamurti V. & Ramanathan S. (2008) Correlation between metal-insulator transition characteristics and electronic structure changes in vanadium oxide thin films. Physical Review B - Condensed Matter and Materials Physics, vol. 77, no. 19, pp. 1-5.

[35] Berglund C.N. & Jayaraman A. (1969) Hydrostatic-pressure dependence of the electronic properties of VO_2 near the semiconductor-metal transition temperature. Physical Review, vol. 185, no. 3, pp. 1034-1039.

[36] Muraoka Y. & Hiroi Z. (2002) Metal-insulator transition of VO_2 thin films grown on TiO_2 (001) and (110) substrates. Applied Physics Letters, vol. 80, no. 4, pp. 583-585.

[37] Cao J. *et al.* (2009) Strain engineering and one-dimensional organization of metal-insulator domains in single-crystal vanadium dioxide beams. Nature Nanotechnology, vol. 4, no. 11, pp. 732-737.

[38] Lopez R., Feldman L.C. & Haglund Jr. R.F. (2004) Size-dependent optical properties of VO_2 nanoparticle arrays. Physical Review Letters, vol. 93, no. 17, pp. 1-4.

[39] Wu J. *et al.* (2006) Strain-induced self organization of metal-insulator domains in single-crystalline VO_2 nanobeams. Nano Letters, vol. 6, no. 10, pp. 2313-2317.

[40] Zhang S., Chou J.Y. & Lauhon L.J. (2009) Direct correlation of structural domain formation with the metal insulator transition in a VO_2 nanobeam. Nano Letters, vol. 9, no. 12, pp. 4527-4532.

[41] Sohn J.I. *et al.* (2009) Surface-stress-induced Mott transition and nature of associated spatial phase transition in single crystalline VO_2 nanowires. Nano Letters, vol. 9, no. 10, pp. 3392-3397.

[42] Tselev A. *et al.* (2010) Symmetry relationship and strain-induced transitions between insulating M1 and M2 and metallic R phases of vanadium dioxide. Nano Letters, vol. 10, no. 11, pp. 4409-4416.

[43] Jones A.C., Berweger S., Wei J., Cobden D. & Raschke M.B. (2010) Nano-optical investigations of the metal-insulator phase behavior of individual VO_2 microcrystals. Nano Letters, vol. 10, no. 5, pp. 1574-1581.

[44] Cao J. *et al.* (2010) Extended mapping and exploration of the vanadium dioxide stress-temperature phase diagram. Nano Letters, vol. 10, no. 7, pp. 2667-2673.

[45] Cullity B.D. (1956) Elements of X-Ray Diffraction. Addison-Wesley, Reading, Mass., 514 p.

[46] Als-Nielsen J. & McMorrow D. (2011) Elements of Modern X-Ray Physics, 2nd Edition. Wiley, Hoboken, 432 p.

[47] Ohring M. (2002) Materials Science of Thin Films, 2nd Edition. Academic Press, San Diego, Calif., 794 p.

[48] Kim D.H. & Kwok H.S. (1994) Pulsed laser deposition of VO_2 thin films. Applied Physics Letters, vol. 65, no. 25, pp. 3188-3190.

[49] Nag J., Payzant E.A., More K.L. & Haglund Jr. R.F. (2011) Enhanced performance of room-temperature-grown epitaxial thin films of vanadium dioxide. Applied Physics Letters, vol. 98, no. 25, pp. 1-3.

[50] Srivastava R. & Chase L.L. (1971) Raman spectrum of semiconducting and metallic VO_2. Physical Review Letters, vol. 27, no. 11, pp. 727-730.

[51] Schilbe P. (2002) Raman scattering in VO_2. Physica B: Condensed Matter, vol. 316-317, pp. 600-602.

[52] Marini C. *et al.* (2008) Optical properties of $V_{1-x}Cr_xO_2$ compounds under high pressure. Physical Review B - Condensed Matter and Materials Physics, vol. 77, no. 23, pp. 1-9.

[53] Ji Y. *et al.* (2014) Role of microstructures on the M1-M2 phase transition in epitaxial VO_2 thin films. Scientific Reports, vol. 4, pp. 1-6.

[54] Okimura K., Sakai J. & Ramanathan S. (2010) In situ x-ray diffraction studies on epitaxial VO_2 films grown on c-Al_2O_3 during thermally induced insulator-metal transition. Journal of Applied Physics, vol. 107, no. 6, pp. 1-5.